Title

Cell-type-specific integration of feedforward and feedback synaptic inputs in the posterior parietal cortex

Journal

Neuron, 110(22)

ISSN

0896-6273

Authors

Rindner, Daniel J

Proddutur, Archana

Lur, Gyorgy

Publication Date

2022-11-01

DOI

10.1016/j.neuron.2022.08.019

Peer reviewed

HHS Public Access

Author manuscript

Neuron. Author manuscript; available in PMC 2023 November 16.

Published in final edited form as:

Neuron. 2022 November 16; 110(22): 3760–3773.e5. doi:10.1016/j.neuron.2022.08.019.

Cell-type specific integration of feedforward and feedback synaptic inputs in the posterior parietal cortex

Daniel J. Rindner[1], **Archana Proddutur**[1], **Gyorgy Lur**[1,#]

[1]Department of Neurobiology and Behavior, University of California, Irvine, 1215 McGaugh Hall, Irvine, CA 92697, USA

Summary

The integration of feedforward (sensory) and feedback (top-down) neuronal signals is a principal function of the neocortex. Yet, we have limited insight into how these information streams are combined by individual neurons. Using a two color optogenetic strategy, we found that layer 5 pyramidal neurons in the posterior parietal cortex receive monosynaptic dual innervation, combining sensory inputs with top-down signals. Subclasses of layer 5 pyramidal neurons integrated these synapses with distinct temporal dynamics. Specifically, regular spiking cells exhibited supralinear enhancement of delayed, but not coincident inputs, while intrinsic burst firing neurons selectively boosted coincident synaptic events. These subthreshold integration characteristics translated to nonlinear summation of action potential firing. Complementing electrophysiology with computational modeling, we found that distinct integration profiles arose from a cell-type specific interaction of ionic mechanisms and feedforward inhibition. These data provide insight into the cellular properties that guide nonlinear interaction of distinct long-range afferents in the neocortex.

eTOC Blurb

Feedforward and feedback pathway interactions are widespread, yet poorly understood. Rindner et al. show that subpopulations of layer 5 pyramidal neurons in the PPC integrate sensory and frontal afferents with distinct nonlinear synaptic dynamics that arise from an interaction of ionic mechanisms and cell type specific feedforward inhibition.

Correspondence: Gyorgy Lur, glur@uci.edu.
[#]Lead Contact

Author contributions: DJR, AP, and GL designed the research, DJR completed and analyzed all *in vitro* physiology experiments, AP conducted all computational modelling. DJR, AP, and GL wrote the manuscript.

Conflict of Interest: The authors declare no conflict of interest.

Supplemental information
Document S1 contains: Figures S1–S10, Tables S1–S2

Introduction

Integrating feedforward and feedback neuronal signals is a principal function of the neocortex. Cortical feedforward systems, originating in primary sensory areas, relay environmental signals to higher order brain structures. These higher order regions in turn send afferents to lower order cortices, forming feedback pathways that carry contextual information like task structure, goals, expectations, and memories. The convergence of feedforward and feedback streams is ubiquitous to most cortical areas and their interaction is fundamental to cognitive processes like attention (Ito et al., 1998; McMains and Kastner, 2011; Morishima et al., 2009; Olson et al., 2001), sensory scene analysis (Habtegiorgis et al., 2019; Snyder et al., 2012), and motor planning (Churchland and Shenoy, 2007; Narayanan and Laubach, 2006; Riehle and Requin, 1989). In sensory regions, feedforward-feedback interactions are thought to contribute to gain control (McAdams and Maunsell, 1999; Moran and Desimone, 1985; Treue and Martinez Trujillo, 1999; Zhang et al., 2014) and the tuning of neuronal receptive fields (Fritz et al., 2003; Li et al., 2004; Spitzer et al., 1988), thereby enabling context-dependent sensory processing. Similar interactions have been observed in the thalamus (O'Connor et al., 2002) and in association cortices (Ibos and Freedman, 2014; Toth and Assad, 2002). Despite this prevalence of feedforward-feedback integration in the neocortex, the synaptic mechanism of how these neuronal pathways interact remains elusive.

According to the canonical circuit model, feedforward projections target granular and infragranular layers of the cortex while feedback axons terminate supragranularly (Kaas et al., 1977; Markov et al., 2014; Rockland and Pandya, 1979; Tigges et al., 1977). Dendritic trees of layer 5 pyramidal neurons vertically span most of the cortex, making them uniquely positioned to integrate contextual information with sensory input (Larkum and Zhu, 2002; Larkum et al., 1999; Llinas et al., 2002; Takahashi et al., 2020; Xu et al., 2012). However, principal cells in layer 5 are not comprised of a homogeneous population. Neuronal categories have been identified via genetic markers, morphology, and electrophysiological properties (Ascoli et al., 2008; Groh et al., 2010; Kim et al., 2015; Oswald et al., 2013; Shepherd, 2013; Tasic et al., 2018). Recent work suggests that this diversity extends to patterns of connectivity, indicating the existence of independent, parallel cortical networks (Anderson et al., 2010; Brown and Hestrin, 2009; Dantzker and Callaway, 2000; Jiang et al., 2015; Morishima et al., 2017). In layer 5, multiple pyramidal cell types have been identified, broadly clustering into regular spiking neurons (RS), typically projecting to other cortical regions and the striatum, and intrinsic burst firing cells (IB) that project subcortically (Chagnac-Amitai et al., 1990; Connors et al., 1982; Dembrow et al., 2010; Gao and Zheng, 2004; Harris and Shepherd, 2015; Hattox and Nelson, 2007; Kasper et al., 1994; Larkman and Mason, 1990; Mason and Larkman, 1990; Morishima et al., 2011; Yang et al., 1996). This segregation of cell types appears to be conserved from mice to humans (Hodge et al., 2019). Previous work demonstrated that these physically interspersed excitatory neurons play distinct roles in encoding sensory stimuli and behavior (Chen et al., 2013; Glickfeld et al., 2013; Kwon et al., 2016; Lur et al., 2016; Tang and Higley, 2020; Yamashita and Petersen, 2016). The two cell types have also been shown to receive unequal excitation in layer 1 (Cauller and Connors, 1994). Accordingly, one recent study found that behavioral

context modulated dendritic signaling in IB, but not in RS neurons (Takahashi *et al.*, 2020). Detailed mapping of synaptic inputs revealed that IB cells in the visual cortex received a greater proportion of their input from the higher order retrosplenial and anterior cingulate cortices than RS neurons (Kim *et al.*, 2015). These data suggest that layer 5 cell types may be differentially regulated by feedforward and feedback information. Nonetheless, whether IB and RS receive direct, monosynaptic innervation from both feedforward and feedback sources, and how these inputs may sum at the synaptic level has yet to be directly examined.

Here, we utilized a two-color optogenetic strategy (Klapoetke et al., 2014), to show that feedforward and feedback synaptic inputs converged onto layer 5 pyramidal neurons in the posterior parietal cortex (PPC). Dual innervated IB and RS neurons displayed distinct nonlinear synaptic integration dynamics that arose from an interaction of multiple ionic mechanisms and cell type specific feedforward inhibition.

Results

Monosynaptic dual innervation of layer 5 PPC neurons by feedforward and feedback afferents

To understand how layer 5 pyramidal neurons in the PPC integrate feedforward inputs with feedback signals, we first set out to determine whether these information streams converge onto individual cells. We expressed the red-shifted channelrhodopsin variant Chrimson in the auditory cortex (AUD, feedforward) and the blue light sensitive channelrhodopsin-2 (ChR2) in the anterior cingulate cortex (ACC, feedback) (Figure 1A). Opsin expressing long-range afferents from ACC and AUD were readily observed in the PPC (Figure 1B). We made whole-cell patch clamp recordings from layer 5 pyramidal neurons in acute PPC slices and used brief pulses of 630nm or 440nm light to activate AUD or ACC axons, respectively (Figure 1C). A caveat of this dual color optogenetic approach is the limited but appreciable sensitivity of Chrimson to blue light (Klapoetke *et al.*, 2014), leading to potential coactivation of afferents by 440nm excitation. To address this issue and ensure input selectivity, we limited blue light pulse duration to 70 μs and determined a maximal power for 440nm excitation that averts opsin cross-activation (Figure S1). In layer 5 of the PPC, we observed similar proportions of intrinsic bursting (IB) and regular spiking (RS) pyramidal neurons (IB 42.3%, RS 57.7%, n = 369, Figure 1D). The two cell types were identified by differences in action potential firing pattern, input resistance, and the magnitude of the depolarizing envelope (initial AP firing: IB 29.4 ± 0.7%, RS 20.6 ± 0.3%, $p < 0.001$; input resistance: IB 61.8 ± 2.1 MΩ, RS 91.1 ± 2.4 MΩ, $p < 0.001$; depolarizing envelope: IB 9.6 ± 0.4 mV, RS 4.4 ± 0.1 mV, $p < 0.001$; IB n = 156, RS n = 213; mean ± SEM; independent samples t-test; Figure 1E and S2A–G). To determine whether inputs were mono- or polysynaptic, we used the TTX/4-AP pharmacological method (Petreanu et al., 2009) (Figure 1F). We found that the application of 4-AP (100–500 μM) after TTX (1 μM) restored glutamatergic synaptic responses to both ACC and AUD afferent activation in the majority of layer 5 cells (Figure 1G, and S2H–K), indicating monosynaptic dual innervation. These experiments suggested that synaptic latencies for verified monosynaptic inputs were no longer than 4 ms (Figure S2L). To distinguish between mono- and polysynaptic inputs and estimate the proportion of dual innervated cells, we applied this 4 ms latency cutoff

to evoked responses in all recorded cells (see Methods). We found that IB and RS neurons were equally likely to receive monosynaptic dual innervation from ACC and AUD afferents (IB 91/107, RS 92/101 cells, p = 0.205, two-sided Fisher's exact test, Figure 1H). We also tested frontal-visual and auditory-visual afferent combinations. IB cells were significantly less likely to receive monosynaptic dual input from ACC and the visual cortex (VIS) than RS neurons (IB 10/16, RS 22/23 cells, p = 0.013, Figure 1I), and were equally likely to receive dual innervation from AUD and VIS (IB 13/15, RS 19/21 cells, p > 0.999, Figure 1J). Only cells receiving monosynaptic dual input (passing the TTX/4AP test or displaying less than 4 ms synaptic latency for both inputs) were included in further analysis. These data suggest that a large proportion of IB and RS neurons in PPC layer 5 receive direct, converging excitation from feedforward and feedback sources.

Temporal profiles of feedforward-feedback integration are cell-type specific

We next sought to determine the temporal dynamics of the interaction between converging feedforward and feedback inputs in IB and RS cells (Figure 2A). We recorded light evoked unimodal EPSPs in response to independent activation of ACC or AUD afferents (Figure 2B and C). Unimodal recordings were interleaved with multimodal trials where the two afferents were co-activated with 0, 50, 100, or 250 ms delay between the light pulses (Figure 2D and E). To quantify synaptic interactions, we calculated a Multimodal Enhancement Index (MEI) by dividing the amplitude of the recorded multimodal response by the summed amplitude of unimodal responses (see Methods). An MEI of 1 would thus indicate linear interaction. By plotting MEI values against the respective synaptic delay, we captured temporal integration profiles for IB and RS cells (Figure 2F and G). In IB cells, coincident activation of ACC and AUD inputs resulted in an evoked response amplitude 34% greater than the linear sum (MEI = 1.34, p = 0.002, n = 12, t-test, Figure 2F). This enhancement was absent when ACC inputs were followed by AUD activation with any delay (50 ms: MEI = 1.06, p = 0.54; 100 ms: MEI = 1.09, p = 0.45; 250 ms: MEI = 0.95, p = 0.56; Figure 2F). Conversely, in RS cells, coincident activation of ACC and AUD inputs resulted in linear integration (MEI = 0.90, p = 0.085, n = 15, t-test, Figure 2G). However, when ACC and AUD inputs arrived at RS cells with a 50–100 ms delay, evoked EPSPs were significantly larger than what linear summation predicted (50 ms: MEI = 1.25, p = 0.005; 100 ms: MEI = 1.20, p = 0.025; 250 ms: MEI = 0.99, p = 0.839; Figure 2G). Two-way ANOVA revealed that IB and RS cells integrate ACC and AUD inputs with distinct temporal dynamics (cell type × synaptic delay interaction $F_{3, 61} = 11.8$, p < 0.0001).

To test whether the sequence of inputs influenced feedforward-feedback interactions, we activated afferents in reverse order: AUD inputs followed by ACC activation (Figure S3A–C). We found that changing the order of inputs had no effect on the temporal dynamics of synaptic integration in either cell type (input order × synaptic delay interaction in IB cells $F_{3, 50} = 0.63$, p = 0.6; in RS cells $F_{3, 73} = 0.21$, p = 0.887; two-way ANOVA). Furthermore, activating AUD and ACC afferents in reverse order preserved the cell-type specificity of integration profiles (cell type × synaptic delay interaction in reversed input order: $F_{3, 62} = 12.38$, p < 0.0001, two-way ANOVA).

A potential caveat of all above experiments is that ChR2 and Chrimson have distinct channel kinetics (Klapoetke *et al.*, 2014), potentially biasing integration dynamics. However, ChR2 and Chrimson evoked EPSP kinetics were indistinguishable across all tested afferents (Figure S3D). Furthermore, temporal dynamics of ACC-AUD integration were not affected by reversing the opsin expression between afferents, i.e., ACC transduced with Chrimson and AUD with ChR2 (opsin target × synaptic delay interaction in IB cells: $F_{3, 50} = 1.33$, $p = 0.28$; in RS cells: $F_{3, 55} = 0.48$, $p = 0.697$; two-way ANOVA; Figure S3E). The observed cell-type specificity of feedforward-feedback synaptic interactions remained robust against changing upstream opsin identities (cell type × synaptic delay interaction $F_{3, 44} = 7.52$, $p = 0.0004$, two-way ANOVA in reverse opsin experiments).

These results demonstrate that the temporal dynamics of nonlinear subthreshold interactions between frontal and auditory inputs are specific to subclasses of layer 5 pyramidal neurons in the PPC.

Distinct combination of ionic mechanisms underpins coincident and delayed supralinearity

Neuronal dendrites are rich in channels that allow for a diverse range of nonlinear computations (Stuart and Spruston, 2015). Among the most well-studied are dendritic spikes caused by regenerative currents through Na^+ channels (Ariav et al., 2003; Golding and Spruston, 1998; Kim and Connors, 1993), Ca^{2+} channels (Golding et al., 1999; Kim and Connors, 1993; Larkum and Zhu, 2002; Losonczy and Magee, 2006; Schiller et al., 1997), or N-methyl-D-aspartate (NMDA) receptors (Polsky et al., 2004; Schiller et al., 2000; Schiller *et al.*, 1997). We explored the interaction of these conductances and their contribution to nonlinear synaptic events in a computational model (see Methods and Figure S4A, B). Feedforward and feedback inputs were modeled as identical glutamatergic synapses as we found no differences between frontal- and sensory-evoked EPSP kinetics (Figure S3D). To determine the role of Na^+, and Ca^{2+}channels, and NMDA receptors in synaptic integration, we independently varied channel conductance or NMDA receptor decay kinetics, while keeping all other parameters fixed. In the resulting 1881 model variants, we calculated MEI values for simulated EPSPs evoked simultaneously or with 50ms delay. We found that increasing Na^+ conductance resulted in the enhancement of coincident inputs (Figure 3A) but had no effect on synaptic integration when synaptic events were delayed by 50 ms (Figure 3B and S4). In contrast, higher Ca^{2+} channel conductance led to enhanced integration of both coincident and delayed inputs (Figure 3A, B, and S4). Varying NMDA receptor decay kinetics had minimal effect on coincident integration but had a marked influence on synaptic interactions at 50 ms delay (Figure 3A, B, and S4).

These results suggest that Na^+ and Ca^{2+} conductances drive supralinear multimodal integration when inputs coincide while the interaction of Ca^{2+} conductance and NMDA receptor decay kinetics determines integration at longer synaptic delays.

Temporal dynamics of synaptic integration are shaped by cell-type specific inhibition

We next asked whether the above mechanisms explained the distinct integration profiles of IB and RS cells. Out of our initial 1881 models (black dots in Figure 3C), 201 variants

(10.6%) captured the observed integration profile of IB cells with a 99% confidence interval (red crosshair). However, no combination of these ionic mechanisms approximated our results from RS cells (blue crosshair, Figure 3C). We thus considered that a non-cell autonomous mechanism may shape the integration profile of these cells. RS neurons have been reported to receive higher inhibitory drive than their IB counterparts (Hefti and Smith, 2000; Sun et al., 2013). Consistent with these findings, we observed stronger feedforward inhibition in RS cells compared to IB neurons (ACC $p = 0.035$; AUD $p = 0.004$; IB $n = 10$, RS $n = 9$; unpaired t-test, Figure 3D, E). The strength of inhibition recruited by ACC and AUD afferents was indistinguishable (IB cells: $p = 0.1$, $n = 10$; RS cells: $p = 0.26$, $n = 9$; paired t-test; Figure 3E). To test the hypothesis that feedforward inhibition shapes the integration profile of RS, but not IB cells, we measured coincident and delayed integration in the presence of the $GABA_A$ receptor antagonist picrotoxin (PTX, 6 μM). We found that PTX had no effect on coincident or delayed ACC-AUD interaction in IB cells (coincident: $p = 0.12$, $n = 11$; 50 ms delay: $p = 0.67$, $n = 10$; Figure 3F). Conversely, in RS neurons, bath application of PTX enhanced coincident integration by 32% (to MEI = 1.24, $p = 0.023$, $n = 11$, paired t-test, Figure 3G) leading to supralinear summation ($p = 0.048$, t-test). Including the non-membrane permeable PTX in the internal solution (10 μM) similarly promoted supralinear coincident integration in RS neurons ($MEI_{iPTX} = 1.23$, $p = 0.02$, $n = 8$, one-sample t-test, Figure 3H and S5F, G). These data suggested that integration of coincident inputs in RS cells was shaped by feedforward inhibition. The relative kinetics of excitation and inhibition measured in RS cells appeared permissive to this interaction (Figure S5A–E). Supralinear delayed (50 ms) integration in RS cells was unaffected by bath applied PTX ($p = 0.42$, $n = 11$, paired t-test; Figure 3G), or by PTX in the pipette solution ($MEI_{50ms,\ iPTX} = 1.44$, $p = 0.005$, $n = 8$, one-sample t-test; Figure 3H). This indicated that inhibition may be reduced when inputs were delayed. Indeed, recording inhibitory postsynaptic currents (IPSCs) evoked by sequential activation of ACC and AUD afferents revealed depressing short-term synaptic dynamics (approximately 39% depression at 50 ms, Figure S6A, B). Thus, we incorporated feedforward inhibition in our computational model (Figure 3I) and calculated the MEI of EPSPs simulated with varying Na^+, Ca^{2+} and NMDA decay parameters. Now including a depressing GABAergic synapse, we generated and additional 1881 model variants (Figure S6C, D), allowing us to capture the integration characteristics of RS neurons (Figure 3C).

In vitro pharmacology confirms model predictions

The above models predict that specific ionic conductances support the enhancement of coincident inputs to IB cells and delayed inputs to RS neurons. To test these predictions, we first created a model cell with medium-high Na^+ (0.065 nS) and Ca^{2+} (0.0048 nS at the proximal dendrite) conductance and fast NMDA decay kinetics ($\tau = 30$ ms) to approximate IB neurons. This model produced supralinear integration of coincident inputs (MEI = 1.38) but linear addition at 50ms delay (MEI = 1.04, Figure 4A and B). Blocking Na^+, Ca^{2+}, or NDMA conductances in the model, resulted in near linear coincident integration ($MEI_{Na\text{-}block}$: 1.08, $MEI_{Ca\text{-}block} = 0.909$, $MEI_{NMDA\text{-}block} = 1.04$ Figure 4A). We then conducted the same experiments *in vitro*, recording ACC-AUD integration in IB neurons while bath applying pharmacological blockers. Supralinear integration of coincident inputs was diminished by bath application of a low-concentration (100 nM) of the Na^+ channel

blocker tetrodotoxin (TTX, MEI reduction of 0.31, p = 0.030, n = 7 cells; paired t-test, Figure 4C). We obtained a similar result in putative IB neurons (projecting to the Pons, Figure S7A–E, Methods) by including the non-membrane permeable Na^+-channel blocker QX 314 (5 mM) in the pipette solution (MEI_{QX} = 0.92, p = 0.37, n = 7, t-test, Figure S7F). Coincident supralinearity was also reduced by the T-type Ca^{2+} channel blocker mibefradil (Mib, 20 μM, 0.20 reduction in MEI, p = 0.013, n = 13; Figure 4C) and to a lesser extent by the NMDA receptor antagonist D-2-amino-5-phosphonovalerate (AP5, 50 μM, 0.18 reduction in MEI, p = 0.034, n = 11; Figure 4C). In IB cells, linear integration at 50 ms synaptic delay was unaffected by any of the tested agents (TTX: p = 0.457, n = 7; Mib: p = 0.52, n = 8; AP5: p = 0.155, n = 11; Figure 4D). Vehicle flow-in for equivalent time periods resulted in no change in synaptic integration in IB cells (Figure S7G).

To simulate coincident and delayed integration in RS cells, we generated a model neuron with low Na^+ conductance (0.015 nS), high Ca^{2+} conductance (0.0062 nS at the proximal dendrite) and slow NMDA receptor decay kinetics (τ = 60 ms). This model RS neuron also included feedforward inhibition targeting the excitatory recipient dendritic segment. The use of longer NMDA receptor decay kinetics in this model was supported by longer decay time constants observed both in EPSPs and NMDA currents of RS neurons *in vitro* (Figure S7I–K). Our RS neuron model, now including inhibition, produced near-linear coincident integration (MEI = 0.90) that was unaffected by blocking Na^+, Ca^{2+} or NMDA conductances (shown in orange in Figure 4E). Similarly to our observations of RS neurons *in vitro*, simulations produced supralinear synaptic interaction when the inputs were delayed by 50 ms (50 ms MEI = 1.22, Figure 4F). Delayed supralinearity persisted in the absence of Na^+ conductance (50 ms $MEI_{Na\text{-}block}$ = 1.22), however, it was abolished by removal of Ca^{2+} or NMDA conductances (50 ms $MEI_{Ca\text{-}block}$ = 0.98, 50 ms $MEI_{NMDA\text{-}block}$ = 1.07, Figure 4F). We then reproduced these experiments *in vitro*, recording AUD-ACC integration in RS neurons while bath applying pharmacological blockers. Coincident integration in RS cells was unaffected by drug treatment (TTX (100 nM): p = 0.687, n = 6; Mib: p = 0.35, n = 8; AP5: p = 0.185, n = 10; paired t-test, Figure 4G). At 50 ms synaptic delay, TTX had no effect on integration (p = 0.511, n = 7; Figure 4H). However, application of both Mib and AP5 significantly reduced multimodal enhancement of delayed inputs (Mib: 0.34 reduction in MEI, p = 0.012, n = 8; AP5: 0.28 reduction in MEI, p = 0.005, n = 11; paired t-test, Figure 4H). Vehicle flow-in did not alter integration in RS cells (Figure S7H).

These data indicate that the expression of high Na^+ and Ca^{2+} conductances combined with fast NMDA receptor decay cause IB neurons to act as coincidence detectors. Conversely, in RS cells, an interaction of high Ca^{2+} conductance and slow NMDA receptor decay kinetics drives supralinear addition of delayed inputs while $GABA_A$ mediated feedforward inhibition linearizes coincident integration.

Subthreshold feedforward-feedback interactions translate to nonlinear action potential firing

To test whether the action potential output of IB and RS cells reflected the observed subthreshold integration dynamics, we adjusted stimulus strength to elicit action potentials in unimodal trials with approximately 50% probability (Figure 5A and B). In interleaved

trials, ACC and AUD afferents were activated either coincidentally, or with a 50, 100, or 250 ms delay (Figure 5C, D). We calculated a suprathreshold MEI by dividing the number of action potentials fired in response to the combined stimulation by the sum of unimodal action potentials. IB cells exhibited supra-additive action potential firing in response to coincident activation of ACC and AUD inputs (MEI = 1.56, p = 0.007, n = 11; t-test; Figure 5E). However, multimodal action potential firing in IB cells was indistinguishable from linear summation when the two inputs were delayed (50 ms: MEI = 1.19, p = 0.308; 100 ms: MEI = 1.11, p = 0.347; 250 ms: MEI = 1.10, p = 0.417; Figure 5E). In contrast, RS cell action potential firing in response to coincident activation of ACC and AUD afferents was linear (MEI = 0.95, p = 0.539, n = 11; t-test, Figure 5F). Multimodal stimulation with 50 ms delay between inputs resulted in supra-additive action potential firing in RS neurons (MEI = 1.33, p = 0.011, n = 11; Figure 5F), while longer delays yielded linear integration (100 ms: MEI = 1.17, p = 0.248; 250 ms: MEI = 0.92, p = 0.457; Figure 5F). Multimodal integration profiles were significantly different between RS and IB neurons (cell type × synaptic delay interaction: $F_{3, 58} = 4.18$, p = 0.0096, two-way ANOVA).

Overall, nonlinear enhancement of action potential firing in response to multimodal stimulation closely mirrored subthreshold synaptic integration in both IB and RS cells.

Input specificity of nonlinear interactions differs between layer 5 cell types

Finally, we sought to determine whether nonlinear multimodal enhancement in layer 5 pyramidal neurons of the PPC is a general feature of long-range afferent interactions or specific to the integration of ACC and AUD inputs. To answer this question, we first expressed ChR2 in the ACC and Chrimson in the visual cortex (VIS, Figure 6A), and measured ACC-VIS synaptic interaction as described above. In IB cells, coincident activation of ACC and VIS inputs resulted in a supralinear enhancement of EPSP amplitude (MEI = 1.30, p = 0.008, n = 8, t-test; Figure 6B), while delayed activation of the two afferents resulted in linear integration (50 ms: MEI = 0.96, p = 0.689; 100 ms: MEI = 1.08, p = 0.259; 250 ms: MEI = 0.95, p = 0.659; Figure 6B). In RS cells, ACC and VIS inputs summed linearly when activated coincidentally (MEI = 1.01, p = 0.841, n = 9; Figure 6C), while 50 and 100 ms delayed activation induced supralinear responses ms: MEI = 1.23, p = 0.016; 100 ms: MEI = 1.31 p = 0.028; 250 ms: MEI = 1.04 p = 0.485; Figure 6C). Two-way ANOVA revealed that IB and RS cells have distinct temporal characteristics for ACC-VIS integration (cell type × synaptic delay interaction $F_{3, 36} = 9.72$, p < 0.0001). Comparison of ACC-AUD and ACC-VIS integration profiles indicated that frontal-sensory interaction dynamics are insensitive to the identity of the sensory input (input combination in IB cells: $F_{3, 43} = 0.15$, p = 0.93; in RS cells: $F_{3, 54} = 0.6173$, p = 0.61; two-way ANOVA). These results suggest that the cell-type specificity of nonlinear synaptic interactions may be a general feature of frontal-sensory integration in the PPC.

Next, we asked whether layer 5 pyramidal neurons in the PPC exhibit nonlinear integration of two sensory inputs. We expressed ChR2 in AUD and Chrimson in VIS afferents (Figure 6D) and measured their interaction as described above. In IB cells, activation of AUD and VIS inputs resulted in linear summation of both coincident (MEI = 1.04, p = 0.647, n = 9; t-test, Figure 6E) and delayed inputs (50 ms: MEI = 1.04, p = 0.290; 100 ms: MEI = 0.98,

p = 0.760; 250 ms: MEI = 0.96, p=0.302; Figure 6E). Comparing the temporal dynamics of frontal-sensory and sensory-sensory interactions indicated that in IB cells, nonlinear synaptic integration is specific to frontal-sensory input combinations (ACC-AUD_{IB} vs. AUD-VIS_{IB} × synaptic delay interaction $F_{3, 49} = 3.28$, p = 0.029; ACC-VIS_{IB} vs. AUD-VIS_{IB} × synaptic delay interaction $F_{3, 42} = 3.23$, p = 0.031, two-way ANOVA). In RS cells, coincident AUD and VIS inputs summed linearly (MEI = 1.00, p = 0.973, n = 15, t-test; Figure 6F) while inputs delayed by 50–100 ms showed enhancement (50 ms: MEI = 1.17, p = 0.034; 100 ms: MEI = 1.21, p = 0.004; 250 ms: MEI = 1.06, p = 0.339; Figure 6F). In contrast to IB cells, frontal-sensory integration profiles in RS neurons were indistinguishable from the sensory-sensory input combination (ACC-AUD_{RS} vs. AUD-VIS_{RS} × synaptic delay interaction $F_{3, 72} = 1.1$, p = 0.35; ACC-VIS_{RS} vs. AUD-VIS_{RS} × synaptic delay interaction $F_{3, 54} = 0.29$, p = 0.84, two-way ANOVA).

These data suggest that RS cells integrate long-range inputs with a similar nonlinear profile while supralinear integration of coincident inputs by IB neurons is specific to feedforward-feedback input combinations.

Synapse location plays a key role in nonlinear interactions

Input specific integration profiles suggested potential differences in how various feedforward and feedback afferents target distinct classes of PPC neurons. To examine this, we first determined the relative location of ACC, AUD and VIS axonal fibers in the PPC as a coarse measure of synapse distribution. We found that in general, all afferents were present throughout the cortical column, although their density varied greatly across the layers (Figure 7A, B). Superficial layers of the PPC (0–150 μm from the pial surface) were enriched in fibers originating from the ACC and AUD. Intermediate layers (150–400 μm) showed high densities of AUD and VIS axons, while all three projections were present in deeper layers (400–800 μm, Figure 7C).

To gain a more detailed insight into how synapse distribution may influence integration in IB and RS cells, we tested multimodal enhancement in seven distinct model configurations. We found that synapse clustering was necessary for multimodal enhancement in both IB and RS (Figure 7D, E) models. When unimodal EPSPs, measured at the soma, were matched for amplitude, clustered synapses produced larger MEI values then distributed synapses on otherwise identical model neurons. Furthermore, we observed larger nonlinearities, both coincident and delayed, when synapses clustered on distal, rather than proximal dendrites (Figure 7D, E). Notably, we found integration characteristics of various model configurations to be dependent on the synaptic conductance targeting each dendritic section (Figure S8A–F). As predicted by the work of others (Branco and Hausser, 2011; Holmes, 1989; Polsky *et al.*, 2004; Tran-Van-Minh et al., 2016), dendrite diameter also played a critical role, with thinner dendrites producing stronger nonlinearities (Figure S8G–J). We found the location of inhibition to have a lesser effect on multimodal enhancement in our models. In model RS cells, inhibition targeting either the soma or the excitatory recipient dendritic segment effectively suppressed coincident enhancement (Figure 7E and Figure S9A, B), with dendrite targeting inhibition exerting a slightly stronger effect in the majority of model configurations (Figure 7E, S9). The effect of inhibition was dependent on the ratio

of excitatory and inhibitory currents (Figure S9A, B). All RS cell models so far assumed that the two long-range afferents targeted the same interneuron, resulting in a depressing short-term dynamic. While this circuit configuration did fit our *in vitro* data best, depressing short-term dynamics, and thus afferent convergence onto the same interneuron, did not appear to be critical for enhanced integration at 50 ms delays in RS neurons (Figure S9C–E).

Together, these data reinforce the notion that clustering of afferent inputs is a prominent driver of enhanced synaptic integration.

Discussion

In this study we demonstrate that layer 5 pyramidal neurons in the PPC integrate feedforward and feedback synaptic inputs with cell-type specific, nonlinear temporal dynamics. Our data suggest that distinct integration profiles are supported by an interaction of Na^+, Ca^{2+} and NMDA conductances and are further shaped by differential inhibitory innervation.

Individual neurons integrate converging long-range afferent pathways

Multimodal interactions have been well documented in cortical circuits (Fritz *et al.*, 2003; Li *et al.*, 2004; McAdams and Maunsell, 1999; Moran and Desimone, 1985; Spitzer *et al.*, 1988; Treue and Martinez Trujillo, 1999), including between frontal-sensory (Zhang *et al.*, 2014) and sensory-sensory (Barraclough et al., 2005; Meredith et al., 1987; Meredith and Stein, 1983; Olcese et al., 2013) neuronal pathways. Transsynaptic tracing experiments using rabies virus (Wall et al., 2010; Wickersham et al., 2007) suggested that long-range inputs conveying these modalities may co-terminate on individual cortical neurons (Kim *et al.*, 2015; Velez-Fort et al., 2014; Wall et al., 2016). Functional assessment of such synapses however, remained technically challenging. The strict anatomical structure of the hippocampus enabled the characterization of how single cells integrated multiple, identified input pathways at the synaptic level (Remy and Spruston, 2007; Takahashi and Magee, 2009). However, in the neocortex, only specialized preparations allowed for direct stimulation of long-range (e.g. thalamic) inputs (Agmon and Connors, 1991; Cruikshank et al., 2002). While electrical stimulation efforts facilitated the mapping of feedforward and feedback circuits in the visual system (Shao and Burkhalter, 1996), the inherent structural complexity of the neocortex (e.g. axons of passage) complicates the interpretation of such experiments. Focal stimulation methods, in combination with optogenetics, allowed the specific and independent activation of identified afferents (Cruikshank et al., 2010; Petreanu *et al.*, 2009; Yang et al., 2013) but until recently, this was restricted to a single pathway. Here, we circumvented these issues by using a two color optogenetic approach (Klapoetke *et al.*, 2014) to selectively manipulate multiple input pathways to the PPC. We show that a high proportion (~80%) of layer 5 pyramidal neurons receive monosynaptic dual innervation from frontal-sensory and sensory-sensory input combinations. This is in line with previous results indicating a high proportion of layer 5 PPC neurons producing multimodal responses (Olcese *et al.*, 2013). Our data suggests that individual cortical neurons, at least in the PPC, are poised to integrate synaptic information from a diversity of long-range sources.

Multimodal enhancement of feedforward-feedback interactions

Two congruent sensory stimuli can produce action potential firing greater than predicted from the linear sum of unimodal responses. This has been shown in the superior colliculus and in cortical regions, including the PPC (Barraclough *et al.*, 2005; Meredith *et al.*, 1987; Meredith and Stein, 1983; Olcese *et al.*, 2013). However, the synaptic events underlying multisensory enhancement and whether its principles could be extended to the interaction of non-sensory pathways remained unknown. We took advantage of the above detailed pathway convergence, to determine how synaptic inputs from two distinct neuronal pathways interact. In our experiments, the majority of layer 5 pyramidal cells in the PPC displayed supralinear integration of sensory and frontal inputs. However, we found marked differences between intrinsic burst firing (IB) and regular spiking (RS) neuronal populations. Action potential firing in response to multimodal stimuli followed the same cell-type specific nonlinear temporal dynamics as subthreshold inputs. These data suggest that nonlinear synaptic interactions at the single neuron level underlie the enhanced multimodal action potential firing observed by others *in vivo*. Furthermore, our findings indicate that principles of multisensory integration may be relevant to the interaction of afferent pathways other than sensory modalities.

An interaction of ionic and circuit mechanisms underlies synaptic integration profiles

The dendritic processes likely underlying nonlinear integration of synaptic inputs have been studied for decades (Magee, 2000; Stuart and Spruston, 2015). Multiple ionic mechanisms have been identified, including regenerative Na^+, Ca^{2+}, and NMDA currents (Ariav *et al.*, 2003; Golding *et al.*, 1999; Golding and Spruston, 1998; Kim and Connors, 1993; Larkum and Zhu, 2002; Losonczy and Magee, 2006; Polsky *et al.*, 2004; Schiller *et al.*, 2000; Schiller *et al.*, 1997). To determine what conductances drove supralinear synaptic integration at different time scales, we utilized a computational approach. We simulated multimodal integration at variable conductances, essentially producing 1881 distinct models, to explore a large parameter space (Marder and Taylor, 2011). Our model predicted that supralinear summation of coincident inputs was predominantly driven by Na^+ and Ca^{2+} conductances. The effect of NMDA receptor block on coincident inputs was likely due to an overall reduction of EPSP size and consequently diminished driving force, rather than a direct effect on synaptic summation. Conversely, we found that supralinear integration of delayed inputs was co-dependent on Ca^{2+} channel conductance and NMDA receptor decay kinetics. The differential involvement of Na^+ and NMDA conductances in faster and slower integration, respectively, makes intuitive sense given the differences in channel kinetics (Almog et al., 2018; Milescu et al., 2010). However, it is important to note that efficient generation of supralinear integration relied on the interaction of multiple ionic mechanisms. These data urge caution in interpreting results from manipulating individual channels: nonlinear events may be diminished by disrupting such interactions, rather than by the specific removal of individual conductances.

While our initial models captured the integration characteristics of IB neurons, no combination of parameters reproduced the physiology of RS cells. This suggested the presence of an additional, non-cell autonomous mechanism. Feedforward inhibition may control the temporal window for synaptic integration (Hausser and Clark, 1997; Naka

and Adesnik, 2016) and consequently modulate multisensory interactions (Olcese *et al.*, 2013). Indeed, computational models incorporating feedforward inhibition captured RS cell integration characteristics. Corroborating findings by others (Hefti and Smith, 2000; Sun *et al.*, 2013), our *in vitro* measurements showed markedly stronger inhibition in RS cells, suggesting a cell-type specific mechanism. A likely candidate to mediate this effect are Parvalbumin expressing interneurons, which have been shown to receive strong input from long-range afferents (Anastasiades et al., 2018; Cruikshank *et al.*, 2010; Gibson et al., 1999; Li et al., 2014). However, the majority of our computational models favored dendrite targeting over perisomatic inhibition. Thus, the specific contribution of various interneuron species to multimodal integration remains a question for future work.

Cell type specific feedforward-feedback integration

Subclasses of layer 5 output neurons have been described in great detail in the past, with differences in anatomical, genetic, electrophysiological, and functional properties (Groh *et al.*, 2010; Jacob et al., 2012; Kim *et al.*, 2015; Lur *et al.*, 2016; Oswald *et al.*, 2013; Takahashi *et al.*, 2020; Tang and Higley, 2020). Differential integration of long-range afferents adds a new aspect to the list of characteristics distinguishing layer 5 cortical neurons. We found two key differences with regards to multimodal integration.

First, IB and RS cells enhanced the interaction of feedforward and feedback inputs at different synaptic delays. Studies in human subjects and non-human primates found that contextual modulation of sensory processing can occur immediately at response onset or following a 30–200 ms delay (Gilbert and Sigman, 2007; Lamme, 1995; Martinez et al., 1999; Vidyasagar, 1998). Our results offer a potential insight into the circuit mechanisms underlying early and late modulation: temporal differences may be reflecting the time scales at which distinct neuronal populations integrate the sensory stream with feedback inputs. How cell type-specific nonlinear integration influences multimodal cognitive processes like prediction error monitoring or multisensory binding is a question for future research.

Second, nonlinear integration in IB cells was selectively engaged by frontal-sensory and not sensory-sensory input combinations. In contrast, RS neurons displayed similar integration profiles regardless of input combination. Nonlinear dendritic processes are most powerful when synaptic inputs are arranged within a branch, not separated by a bifurcation point (Polsky *et al.*, 2004), and can vary across individual branches (Harnett et al., 2013; Lafourcade et al., 2022). One possible explanation for cell-type specific afferent interactions is that auditory and visual afferents target distinct dendritic branches in IB cells, preventing cross-modal interactions. Our modeling and anatomical data enables such configurations, although we remain agnostic about precise synaptic targeting. Localization of differentially orientation-tuned synapses on L2/3 neurons has been examined in the primary visual cortex (Jia et al., 2010). However, how multimodal synapses are organized on the dendrites of cortical neurons remains an important future question (Larkum and Nevian, 2008).

STAR Methods

RESOURCE AVAILABILITY

Lead contact—Further information and requests for resources should be directed to Gyorgy Lur (glur@uci.edu).

Materials availability—This study did not generate new unique reagents.

Data and code availability

- All data reported in this paper will be shared by the lead contact upon request.
- All analysis code is available on GitHub: https://github.com/LurLab-UCI/Rindner-et-al.-2022. Computational models have been deposited to modelDB: http://modeldb.yale.edu/267509.
- Any additional information required to reanalyze the data reported in this paper is available from the lead contact upon request.

EXPERIMENTAL MODEL AND SUBJECT DETAILS

Experiments were conducted in male and female mice – C57 BL/6J or Ai14 (JAX: 007914). Mice were group housed (up to 4 animals per cage) with *ad libitum* access to food and water under a 12-hour light-dark cycle. AAV injections were made at postnatal day (p) 25–40, slice preparation and recording occurred at p45–60. Animals were randomly assigned to experimental groups, typically litter mates split between at least two conditions. No differences were detected between sexes thus data were pooled. All experiments were performed in accordance with the NIH guidelines on the care and use of laboratory animals and approved by the Institutional Animal Care and Use Committee (AUP 20–076).

METHOD DETAILS

Optogenetic construct expression—For independent control of distinct synaptic inputs to the PPC, we expressed the blue light-sensitive channelrhodopsin ChR2 alongside the red light-sensitive Chrimson (Klapoetke *et al.*, 2014) in separate afferent populations. ChR2 and Chrimson were introduced via transcranial injection of adeno-associated virus (AAV) constructs AAV2.1-Syn-hChR2(H134R)-EYFP (titer: 2.1 × 10^12, Addgene: 26973-AAV1) or AAV2.9-Syn-hChR2(H134R)-EYFP (titer: 3.6 × 10^12, Addgene: 26973-AAV9) for ChR2 (Zhang et al., 2010), and AAV2.1-Syn-ChrimsonR-tdTomato (titer: 2.1 × 10^12, Addgene: 59171-AAV1) or AAV2.9-hSyn-ChrimsonR-tdTomato (titer: 2.9 × 10^12, Addgene: 59171-AAV9) for Chrimson (Klapoetke *et al.*, 2014). Opsin constructs were injected at volumes of 150nL into AUD, 150nL into VIS, 200 nL into ACC. Virus titers and volumes were kept unchanged throughout the experimental series. Mice were injected under isoflurane anesthesia at postnatal day 25–40 (P25 - P40). Injections were targeted to either the anterior cingulate cortex (ACC, coordinates from bregma: anterior-posterior +1.0 mm, medial-lateral 0.3 mm, dorsal-ventral 1.0 mm), auditory cortex (AUD, anterior-posterior −2.8 mm, medial-lateral 4.1 mm, dorsal-ventral 0.8 mm), or visual cortex (VIS, anterior-posterior −3.5 mm, medial-lateral 2.1 mm, dorsal-ventral 0.5 mm).

Opsins were allowed to express for a minimum of 14 – 30 days before physiology experiments. To confirm expression and check for potential retrograde or spillover labeling of PPC neurons, ChR2-EYFP and Chrimson-tdTomato positive afferents were visualized in acute PPC slices via band-pass illumination using an X-Cite mercury lamp (Excelitas Technologies). Slices with overall low expression, with a notable difference of expression between the two opsins, or with PPC neurons expressing either construct, were discarded. To acquire images of ChR2-EYFP- and Chrimson-tdTomato-expressing axons for post-hoc validaton, we fixed acute slices used for physiology experiments in 4% paraformaldehyde dissolved in phosphate-buffered saline for 4 hours before mounting on microscope slides with Prolong containing DAPI (ThermoFisher). Images were taken on a BZ-9000 fluorescence microscope (Keyence).

Electrophysiology—For physiology recordings, 300 μm thick coronal brain slices containing the PPC were prepared on a vibrating microtome (smz7000–2, Campden Instruments) from P45 - P60 mice. Immediately after sectioning, slices were maintained at 32°C for 15 minutes in solution comprised of (in mM): 110 choline, 25 $NaHCO_3$, 1.25 NaH_2PO_4, 3 KCl, 7 $MgCl_2$, 0.5 $CaCl_2$, 10 glucose, 11.6 sodium ascorbate and 3.1 sodium pyruvate, and bubbled with 95% O_2 and 5% CO_2. Slices then were allowed to recover for at least 20 minutes in oxygenated room-temperature ACSF containing (in mM): 126 NaCl, 25 $NaHCO_3$, 10 Glucose, 3 KCl, 2 $CaCl_2$, 1.25 NaH_2PO_4, and 1 $MgSO_4$ prior to recording.

All experiments were conducted close to physiological temperature (32–34 °C) in a submersion type recording chamber mounted on an Olympus BX61-WI microscope. The hippocampus was used as a histological landmark to identify PPC in coronal sections. Recordings were targeted to the mediolateral section of PPC between 1300–1800 μm from the midline to minimize influence of potential subregion-specific differences. This approach resulted in targeting the approximate coordinates of (in mm from the Bregma) AP: 2.0, ML: 1.3–1.8, DV: 0.5–0.65. Whole-cell patch-clamp recordings were obtained from layer 5 pyramidal cells (450–650 μm from the pial surface) identified with video-infrared / differential interference contrast microscopy. For current-clamp recordings, glass electrodes (2–4 MΩ) were filled with internal solution containing (in mM): 135 $KMeSO_3$, 10 HEPES, 4 $MgCl_2$, 4 Na_2ATP, 0.4 NaGTP, and 10 sodium creatine phosphate, and adjusted to pH 7.3 with KOH. To record NMDA currents, K^+ was substituted for Cs^+ to improve space clamp. Series resistance was 9–16 MΩ. Recordings outside of this range, or if series resistance changed more that 20% over the course of the experiment, were discarded. Subthreshold integration experiments were performed in current clamp at a steady-state membrane potential held close to the estimated reversal potential for inhibitory currents (−75 mV). Suprathreshold experiments were performed with a pre-stimulus membrane potential of −60 mV. Voltage clamp measurements of AMPA receptor currents were conducted at −70 mV, NMDA currents were measured at +40 mV and inhibitory currents at 0 mV membrane potential. Signals were amplified using a MultiClamp 700B amplifier (Molecular Devices). Data were sampled at 10 kHz, filtered at 4 kHz, and digitized on National Instruments DAQ boards. WaveSurfer software written in Matlab (HHMI Janelia Research Campus) was used for data acquisition. Offline analysis was performed using custom routines in Python 3.7.

Dual-color optogenetic stimulation—In order to deliver dual-color excitation through the microscope objective, we introduced a 440 nm (blue) and a 630 nm (red) LED (Sutter Instruments) into the light path of the BX61 WII microscope via an optical beam combiner (Lambda OBC, Sutter Instruments). Stimulus duration and amplitude were controlled via the WaveSurfer stimulus library with a stimulus sampling rate of 100 kHz. To determine the LED power windows that avoid cross-excitation of the two opsins, we transduced AUD with either ChR2 or Chrimson in separate animals (single opsin expression). Following at least two weeks of expression, we made whole cell recordings of layer 5 pyramidal neurons in acute PPC slices. We recorded evoked EPSPs in response to independently activating the 440 nm and 630 nm LEDs. We plotted ChR2 and Chrimson mediated postsynaptic responses to each wavelength against the corresponding LED power, measured post-hoc with a light meter (Thorlabs). These measurements outlined the excitation power window for the 440 nm LED that enables the separation of input pathways.

To account for potential differences in expression levels in dual opsin containing mice (both ChR2 and Chrimson in the same preparation), LED power on both channels was adjusted to elicit ~4 mV EPSPs in subthreshold experiments or trigger action potentials on 40–50% of trials in suprathreshold experiments. LED powers were determined for each cell approximately 5 minutes after break-in and kept constant for the duration of the experiment. Unimodal blue and red stimuli were sequentially interleaved with dual activation throughout the full length of each recording.

Cell type classification—PPC layer 5 pyramidal neurons were classified as either intrinsically bursting (IB) or regular spiking (RS) cells based on membrane potential responses to 500 ms step current injections. We measured resting membrane potential, input resistance, sag potential, depolarizing envelope, initial burst, slow afterhyperpolarization (sAHP), and action potential (AP) half-width (Figure S2). Input resistance was determined from a −150 pA step. Sag was calculated as the voltage difference between peak and steady-state hyperpolarization and expressed as a percentage of peak response. Depolarizing envelope was quantified as the maximum difference between the afterhyperpolarization potential of two spikes. Initial burst refers to the percentage of action potentials fired within 40 ms of the first spike. sAHP reflects the potential difference between the pre-step baseline and 400 ms after cessation of a 350 pA step. Cells that had a combination of low input resistance, high initial burst value, larger sag, and larger depolarizing envelope were classified as intrinsic bursting (IB). Cells with high input resistance, low initial burst value, lower sag, and smaller depolarizing envelope were deemed regular spiking (RS). While at the population level there is overlap between these measures, at the level of individual cells, the combination of these metrics separates IB and RS cells. Cell type assignment was performed during *post hoc* analyses, blind to experimental condition or results.

In a subset of experiments, cell-types were identified based on anatomical projection patterns. To do this, we utilized one of three methods. First, in wild type mice, we injected green (488 nm) or red (555 nm) Alexa Fluor-conjugated cholera toxin subunit B (CTB, ThermoFisher) into the dorsal Striatum (350 nl, AP: 0.85, ML: 1.5, DV: 2.0 in mm from Bregma) or into the Pons (500 nl, AP: −4.1, ML: 0.8, DV: 5.5 in mm from Bregma) prepared according to the description in (Conte et al., 2009). Second, in wild type mice, we

transduced the dorsal Striatum or the Pons with AAVrg-hSyn-mCherry (titer: 2.0 × 10^12, volume: 500 nl, Addgene: 114472-AAVrg). Third, in the Ai14 mouse line (JAX: 007914), we transduced the dorsal Striatum or the Pons with pENN.AAV.hSyn.Cre.WPRE.hGH (titer: 1.2 × 10^12, volume: 500 nl, Addgene: 105553-AAVrg) (Cearley et al., 2008). The retrograde constructs were injected at volumes of 350 nL into dStr, and 500 nL into Pons.

Testing monosynaptic inputs—To determine whether afferent inputs were monosynaptic, we utilized a combination of two methods. In a subset of experiments, we performed a pharmacological test following integration measurements, using TTX (Tocris) and 4-Aminopyridine (4-AP, Tocris) (Petreanu *et al.*, 2009). Inputs were considered monosynaptic if the EPSP could be recovered in 4-AP (100–500 μM) after 1 μM TTX application. After recovery, we applied a combination of AMPA- and NMDA receptor blockers – 2,3-Dioxo-6-nitro-1,2,3,4-tetrahydrobenzo[f]quinoxaline-7-fulfonamide (NBQX, 10 μM, Tocris) and 2-amino-5-phosphonopentanoic acid (AP5, 50 μM, Tocris), respectively – to confirm synaptic responses were indeed glutamatergic. The shortest EPSP latency, measured prior to TTX application, of inputs failing the TTX/4-AP test was 4.0 ms. Thus, we chose 4 ms as our latency cutoff which was then applied *post hoc* to all experiments. Recordings where inputs failed either the pharmacological or latency test were removed from further analyses.

Histology—Afferent fibers in the PPC were visualized via the EYFP and tdTomato fluorescent tags on the ChR2 and ChrimsonR constructs, respectively. Projection neurons were identified for histology using Alexa Flour 555 or 488 conjugated CTB. After 14–30 days of opsin expression, (7–10 days for CTB) mice were deeply anesthetized using isoflurane and transcardially perfused with 4% paraformaldehyde (PFA) in Sorenson's buffer. Brains were extracted and post-fixed in 4% PFA overnight. Coronal slices (50 μm) were prepared on a vibrating microtome (Compresstome, Precisionary Instruments). Slices were mounted on gelatin coated microscope slides and cover slips were affixed with Prolong Diamond (ThermoFisher). Neurons throughout the tissue were visualized via NeuroTrace 435/455 fluorescent Nissl staining (ThermoFisher). Some slices without NeuroTrace staining were instead mounted with Prolong containing DAPI.

Samples were imaged on a Zeiss LSM900 confocal microscope using a 20x air immersion objective and appropriate filter sets. Tiled images were assembled, and channels assigned faux color in the Zen software (Zeiss).

Fluorescent intensities throughout the cortical column were quantified using the plot profile tool in ImageJ with a line width of 100 pixels. Intensities were normalized to peak fluorescence within each measurement. We used the integral of mean fluorescence to compare the relative density of ACC, AUD, and VIS afferents in superficial (0–150 μm), intermediate (150–400 μm), and deep (400–800 μm) cortical layers.

Drugs and salts—For pharmacological experiments, drug effects were recorded at 5–10 minutes after the addition of the compounds to the perfusion fluid. Agents were used at the following concentrations: mibefradil (Tocris): 20 μM, 2-amino-5-phosphonopentanoic acid (AP5, Tocris): 50 μM, tetrodotoxin (TTX, Tocris): 100 nM, picrotoxin (PTX, Tocris):

6 μM, NBQX (Tocris): 10 μM, 4-AP (Tocris): 100–500 μM. For cell autonomous inhibition of Na^+ channels, QX 314 (HelloBio) was added to the intracellular solution in 5 mM concentration. To specifically block postsynaptic $GABA_A$ receptors, we included picrotoxin in the pipette solution at 10 μM concentration (Inomata et al., 1988; Metherate and Ashe, 1993; Yazaki-Sugiyama et al., 2009). All other materials, including standard salts, were acquired from Sigma or Fisher Scientific.

Computational modeling of synaptic interactions—We produced a compartmental model in the NEURON simulation environment (Hines and Carnevale, 1997), that included a soma and dendrites with a proximal and distal component. Each dendritic segment had a length of 150 μm and diameter of 1 μm with additional models testing 0.5 and 2 μm dendritic diameters. The somatic compartment had a length of 15 μm and diameter of 15 μm. Two morphologies were tested: a simple arrangement with one dendrite attached to the soma and a more complex morphology with two identical dendrites, both originating from the soma. Passive properties of the model cell include input resistance: 94.8 MΩ; axial resistance: 100 Ω·m; capacitance of each compartment: 1.5 $\mu F/cm^2$; leak channel conductance: 0.9 mS/cm^2 with a reversal potential of −70 mV. The resting membrane potential of the model cell was −68 mV. Ion channel conductances were distributed in the compartments as described in Table S1. Sodium and potassium channel conductances (gNa and gK) were uniformly distributed (Morgan et al., 2007) whereas low threshold T-type calcium channel conductance (gT-Ca) distribution was highest in the proximal dendritic segment in a 1 : 2 : 1 = soma : proximal : distal ratio (Destexhe et al., 1998; Zomorrodi et al., 2008). A calcium-dependent potassium channel conductance (gSK) was evenly distributed in all segments. We also included a hyperpolarization-activated potassium conductance modeled after the HCN1 channel (gHCN1) distributed with concentration increasing towards the distal dendrite (Harnett et al., 2015; Stadler et al., 2014). See all conductance values and model details in Table S1.

To simulate frontal and sensory inputs, glutamatergic excitatory synapses were placed in the dendritic compartments as indicated in the figure schematics and were driven via NetCon objects. They included AMPA and NMDA receptor-mediated conductances and were modeled with exponential rise and decay kinetics using the Exp2Syn class, as adapted from (Egger et al., 2015). AMPA receptor current rise and decay time constants (τ) were 0.2 and 2 ms, respectively. NMDA receptor currents had a τ_{rise} = 4 ms, while the τ_{decay} parameter was varied from 30–70 ms in increments of 5ms (Schulz et al., 2018). AMPA and NMDA receptor maximal conductance was varied between 2–4 nS to explore the conductance dependence of synaptic interactions in Figure S8. Conversely, to compare the performance of various model configurations in Figure 7, conductances were adjusted to produce identical unimodal EPSP magnitudes across morphologies. Where described, we also included an inhibitory $GABA_A$ receptor synapse on either the dendritic segment targeted by excitation or on the soma. $GABA_A$ receptor synapses had rise and decay kinetics of τ_{rise} = 0.5 ms and τ_{decay} = 20 ms, with conductance matching the conductance of the respective excitatory synapses (Egger *et al.,* 2015). To represent the short-term depression of $GABA_A$ synaptic inputs we reduced the maximal conductance of delayed inhibitory inputs in the model by 40%, mimicking values observed in our physiology experiments.

The reversal potential of $GABA_A$ receptor synapses was set to −75 mV after our calculated chloride reversal potential. To mimic conditions of our in vitro experiments, the model cell was clamped at −75 mV for the duration of synaptic integration simulations. Two individual VecStim Pointprocess objects were used to simulate frontal and sensory input synapses, which were activated either alone (unimodal), or together with a 0 ms or 50 ms delay (multimodal). Antagonistic drug effects were simulated by setting target conductances to 0 S (simulated TTX, gNA = 0 S; simulated mibefradil, gT-Ca = 0 S, gSK = 0 S; simulated AP5, gNMDAR = 0 S). Multimodal enhancement index (MEI) of each simulated integration events was calculated exactly as was for physiology experiments (see below). In some model configurations, high excitatory conductance drove the model to spike. In these cases, we calculated MEI using the action potential threshold calculated using first derivative method (dV/dt) where membrane potential reached ~10mV/ms. We extracted membrane potential traces of individual simulations and measured spike threshold using dV/dt method in the Clampfit Software. While this calculation likely underestimated the true supralinearity produced by the synaptic integration, we judged it to be the most physiologically relevant readout.

QUANTIFICATION AND STATISTICAL ANALYSIS

Experimental design and statistical analysis—In all figures, we present all recorded data points, the data mean and 95% confidence intervals. Up to three cells were recorded per animal for each experiment. Responses recorded from the same cell type within an animal were then averaged and treated as a single experimental replicate (n) for all statistical comparisons unless specifically stated otherwise (for a detailed breakdown of cell and animal numbers in main Figures see Table S2). Cell type assignment was performed blind to experimental condition (see Cell type classification above). Assessment of drug effects were performed within cells (pre and post drug conditions) using paired t-test. In this case, no more than two replicates were recorded from a single animal. Feedforward inhibition to L5 cells was calculated from evoked EPSPs as the voltage difference before and after $GABA_A$ blockade (PTX, 6 μM) at the time of peak in PTX. Means, confidence intervals and t-statistics were calculated in Python 3.7. Where applicable, multiple comparisons were accounted for using Sidak's correction.

Temporal dynamics of synaptic interaction were analyzed by comparing the recorded multimodal response amplitude to the arithmetic sum of unimodal EPSPs at the corresponding delay using a one-sample t-test. Integration profiles across groups were compared using a mixed model two-way ANOVA in Prism 8 (GraphPad). Given that we found no effect of input order on subthreshold integration profiles, action potential firing data from each cell were pooled and averaged across input orders.

To handle datasets with particularly large variance, Mahalanobis distance-based outlier detection with a cutoff of 0.80 was applied to experiments with suspected outliers. This pertains to subpanels in Figure 4F, Figure 5D. Main text versions of these figures display data after outlier removal. All recorded datapoints for the above experiments, including outliers, are presented in Figure S10. Statistical comparisons in the main text represent those made after excluding outliers. The legend of Figure S10 contains statistical comparisons

made using all recorded datapoints. These highlight that removing outliers resulted in cosmetic changes only and did not alter any results or conclusions.

Quantification of multimodal interactions—To quantify the interaction of two distinct synaptic inputs, we calculated a Multimodal Enhancement Index (MEI) by dividing the recorded multimodal response by the arithmetic sum of unimodal responses. Subthreshold MEI was calculated using evoked EPSP amplitudes: $EPSP_{multimodal}$ / ($EPSP_{unimodal\text{-}1}$ + $EPSP_{unimodal\text{-}2}$), where the sum of unimodal responses was determined by adding the voltage traces resulting from each unimodal stimulation. Suprathreshold MEI was calculated using the number of evoked action potentials (APs): $nAP_{multimodal}$ / ($nAP_{unimodal\text{-}1}$ + $nAP_{unimodal\text{-}2}$).

Supplementary Material

Refer to Web version on PubMed Central for supplementary material.

Acknowledgements:

These studies were funded by the Whitehall Foundation: 2018–12-09 (GL), the NIMH: R01MH123686 (GL), the NINDS: R01NS127785 (GL) and NIDCD: T32DC010775–12 (DJR). We thank the Optical Biology Core Facility of the Developmental Biology Center, a shared resource supported by the Cancer Center Support Grant (CA-62203) and Center for Complex Biological Systems Support Grant (GM-076516) at the University of California, Irvine.

References

Agmon A, and Connors BW (1991). Thalamocortical responses of mouse somatosensory (barrel) cortex in vitro. Neuroscience 41, 365–379. 10.1016/0306-4522(91)90333-j. [PubMed: 1870696]

Almog M, Barkai T, Lampert A, and Korngreen A (2018). Voltage-Gated Sodium Channels in Neocortical Pyramidal Neurons Display Cole-Moore Activation Kinetics. Front Cell Neurosci 12, 187. 10.3389/fncel.2018.00187. [PubMed: 29997481]

Anastasiades PG, Marlin JJ, and Carter AG (2018). Cell-Type Specificity of Callosally Evoked Excitation and Feedforward Inhibition in the Prefrontal Cortex. Cell Rep 22, 679–692. 10.1016/j.celrep.2017.12.073. [PubMed: 29346766]

Anderson CT, Sheets PL, Kiritani T, and Shepherd GM (2010). Sublayer-specific microcircuits of corticospinal and corticostriatal neurons in motor cortex. Nat Neurosci 13, 739–744. 10.1038/nn.2538. [PubMed: 20436481]

Ariav G, Polsky A, and Schiller J (2003). Submillisecond precision of the input-output transformation function mediated by fast sodium dendritic spikes in basal dendrites of CA1 pyramidal neurons. J Neurosci 23, 7750–7758. [PubMed: 12944503]

Ascoli GA, Alonso-Nanclares L, Anderson SA, Barrionuevo G, Benavides-Piccione R, Burkhalter A, Buzsaki G, Cauli B, Defelipe J, Fairen A, et al. (2008). Petilla terminology: nomenclature of features of GABAergic interneurons of the cerebral cortex. Nat Rev Neurosci 9, 557–568. 10.1038/nrn2402. [PubMed: 18568015]

Barraclough NE, Xiao D, Baker CI, Oram MW, and Perrett DI (2005). Integration of visual and auditory information by superior temporal sulcus neurons responsive to the sight of actions. J Cogn Neurosci 17, 377–391. 10.1162/0898929053279586. [PubMed: 15813999]

Branco T, and Hausser M (2011). Synaptic integration gradients in single cortical pyramidal cell dendrites. Neuron 69, 885–892. 10.1016/j.neuron.2011.02.006. [PubMed: 21382549]

Brown SP, and Hestrin S (2009). Intracortical circuits of pyramidal neurons reflect their long-range axonal targets. Nature 457, 1133–1136. 10.1038/nature07658. [PubMed: 19151698]

Cauller LJ, and Connors BW (1994). Synaptic physiology of horizontal afferents to layer I in slices of rat SI neocortex. J Neurosci 14, 751–762. [PubMed: 7905516]

Cearley CN, Vandenberghe LH, Parente MK, Carnish ER, Wilson JM, and Wolfe JH (2008). Expanded repertoire of AAV vector serotypes mediate unique patterns of transduction in mouse brain. Mol Ther 16, 1710–1718. 10.1038/mt.2008.166. [PubMed: 18714307]

Chagnac-Amitai Y, Luhmann HJ, and Prince DA (1990). Burst generating and regular spiking layer 5 pyramidal neurons of rat neocortex have different morphological features. J Comp Neurol 296, 598–613. 10.1002/cne.902960407. [PubMed: 2358553]

Chen JL, Carta S, Soldado-Magraner J, Schneider BL, and Helmchen F (2013). Behaviour-dependent recruitment of long-range projection neurons in somatosensory cortex. Nature 499, 336–340. 10.1038/nature12236. [PubMed: 23792559]

Churchland MM, and Shenoy KV (2007). Delay of movement caused by disruption of cortical preparatory activity. J Neurophysiol 97, 348–359. 10.1152/jn.00808.2006. [PubMed: 17005608]

Connors BW, Gutnick MJ, and Prince DA (1982). Electrophysiological properties of neocortical neurons in vitro. J Neurophysiol 48, 1302–1320. 10.1152/jn.1982.48.6.1302. [PubMed: 6296328]

Conte WL, Kamishina H, and Reep RL (2009). The efficacy of the fluorescent conjugates of cholera toxin subunit B for multiple retrograde tract tracing in the central nervous system. Brain Struct Funct 213, 367–373. 10.1007/s00429-009-0212-x. [PubMed: 19621243]

Cruikshank SJ, Rose HJ, and Metherate R (2002). Auditory thalamocortical synaptic transmission in vitro. J Neurophysiol 87, 361–384. 10.1152/jn.00549.2001. [PubMed: 11784756]

Cruikshank SJ, Urabe H, Nurmikko AV, and Connors BW (2010). Pathway-specific feedforward circuits between thalamus and neocortex revealed by selective optical stimulation of axons. Neuron 65, 230–245. 10.1016/j.neuron.2009.12.025. [PubMed: 20152129]

Dantzker JL, and Callaway EM (2000). Laminar sources of synaptic input to cortical inhibitory interneurons and pyramidal neurons. Nat Neurosci 3, 701–707. 10.1038/76656. [PubMed: 10862703]

Dembrow NC, Chitwood RA, and Johnston D (2010). Projection-specific neuromodulation of medial prefrontal cortex neurons. J Neurosci 30, 16922–16937. 10.1523/JNEUROSCI.3644-10.2010. [PubMed: 21159963]

Destexhe A, Neubig M, Ulrich D, and Huguenard J (1998). Dendritic low-threshold calcium currents in thalamic relay cells. J Neurosci 18, 3574–3588. [PubMed: 9570789]

Egger R, Schmitt AC, Wallace DJ, Sakmann B, Oberlaender M, and Kerr JN (2015). Robustness of sensory-evoked excitation is increased by inhibitory inputs to distal apical tuft dendrites. Proc Natl Acad Sci U S A 112, 14072–14077. 10.1073/pnas.1518773112. [PubMed: 26512104]

Fritz J, Shamma S, Elhilali M, and Klein D (2003). Rapid task-related plasticity of spectrotemporal receptive fields in primary auditory cortex. Nat Neurosci 6, 1216–1223. 10.1038/nn1141. [PubMed: 14583754]

Gao WJ, and Zheng ZH (2004). Target-specific differences in somatodendritic morphology of layer V pyramidal neurons in rat motor cortex. J Comp Neurol 476, 174–185. 10.1002/cne.20224. [PubMed: 15248197]

Gibson JR, Beierlein M, and Connors BW (1999). Two networks of electrically coupled inhibitory neurons in neocortex. Nature 402, 75–79. 10.1038/47035. [PubMed: 10573419]

Gilbert CD, and Sigman M (2007). Brain states: top-down influences in sensory processing. Neuron 54, 677–696. 10.1016/j.neuron.2007.05.019. [PubMed: 17553419]

Glickfeld LL, Andermann ML, Bonin V, and Reid RC (2013). Cortico-cortical projections in mouse visual cortex are functionally target specific. Nat Neurosci 16, 219–226. 10.1038/nn.3300. [PubMed: 23292681]

Golding NL, Jung HY, Mickus T, and Spruston N (1999). Dendritic calcium spike initiation and repolarization are controlled by distinct potassium channel subtypes in CA1 pyramidal neurons. J Neurosci 19, 8789–8798. [PubMed: 10516298]

Golding NL, and Spruston N (1998). Dendritic sodium spikes are variable triggers of axonal action potentials in hippocampal CA1 pyramidal neurons. Neuron 21, 1189–1200. 10.1016/s0896-6273(00)80635-2. [PubMed: 9856473]

Groh A, Meyer HS, Schmidt EF, Heintz N, Sakmann B, and Krieger P (2010). Cell-type specific properties of pyramidal neurons in neocortex underlying a layout that is modifiable depending on the cortical area. Cereb Cortex 20, 826–836. 10.1093/cercor/bhp152. [PubMed: 19643810]

Habtegiorgis SW, Jarvers C, Rifai K, Neumann H, and Wahl S (2019). The Role of Bottom-Up and Top-Down Cortical Interactions in Adaptation to Natural Scene Statistics. Front Neural Circuits 13, 9. 10.3389/fncir.2019.00009. [PubMed: 30814934]

Harnett MT, Magee JC, and Williams SR (2015). Distribution and function of HCN channels in the apical dendritic tuft of neocortical pyramidal neurons. J Neurosci 35, 1024–1037. 10.1523/JNEUROSCI.2813-14.2015. [PubMed: 25609619]

Harnett MT, Xu NL, Magee JC, and Williams SR (2013). Potassium channels control the interaction between active dendritic integration compartments in layer 5 cortical pyramidal neurons. Neuron 79, 516–529. 10.1016/j.neuron.2013.06.005. [PubMed: 23931999]

Harris KD, and Shepherd GM (2015). The neocortical circuit: themes and variations. Nat Neurosci 18, 170–181. 10.1038/nn.3917. [PubMed: 25622573]

Hattox AM, and Nelson SB (2007). Layer V neurons in mouse cortex projecting to different targets have distinct physiological properties. J Neurophysiol 98, 3330–3340. 10.1152/jn.00397.2007. [PubMed: 17898147]

Hausser M, and Clark BA (1997). Tonic synaptic inhibition modulates neuronal output pattern and spatiotemporal synaptic integration. Neuron 19, 665–678. 10.1016/s0896-6273(00)80379-7. [PubMed: 9331356]

Hefti BJ, and Smith PH (2000). Anatomy, physiology, and synaptic responses of rat layer V auditory cortical cells and effects of intracellular GABA(A) blockade. J Neurophysiol 83, 2626–2638. 10.1152/jn.2000.83.5.2626. [PubMed: 10805663]

Hines ML, and Carnevale NT (1997). The NEURON simulation environment. Neural Comput 9, 1179–1209. 10.1162/neco.1997.9.6.1179. [PubMed: 9248061]

Hodge RD, Bakken TE, Miller JA, Smith KA, Barkan ER, Graybuck LT, Close JL, Long B, Johansen N, Penn O, et al. (2019). Conserved cell types with divergent features in human versus mouse cortex. Nature 573, 61–68. 10.1038/s41586-019-1506-7. [PubMed: 31435019]

Holmes WR (1989). The role of dendritic diameters in maximizing the effectiveness of synaptic inputs. Brain Res 478, 127–137. 10.1016/0006-8993(89)91484-4. [PubMed: 2538199]

Ibos G, and Freedman DJ (2014). Dynamic integration of task-relevant visual features in posterior parietal cortex. Neuron 83, 1468–1480. 10.1016/j.neuron.2014.08.020. [PubMed: 25199703]

Inomata N, Tokutomi N, Oyama Y, and Akaike N (1988). Intracellular picrotoxin blocks pentobarbital-gated Cl- conductance. Neurosci Res 6, 72–75. 10.1016/0168-0102(88)90007-7. [PubMed: 3264396]

Ito M, Westheimer G, and Gilbert CD (1998). Attention and perceptual learning modulate contextual influences on visual perception. Neuron 20, 1191–1197. 10.1016/s0896-6273(00)80499-7. [PubMed: 9655506]

Jacob V, Petreanu L, Wright N, Svoboda K, and Fox K (2012). Regular spiking and intrinsic bursting pyramidal cells show orthogonal forms of experience-dependent plasticity in layer V of barrel cortex. Neuron 73, 391–404. 10.1016/j.neuron.2011.11.034. [PubMed: 22284191]

Jia H, Rochefort NL, Chen X, and Konnerth A (2010). Dendritic organization of sensory input to cortical neurons in vivo. Nature 464, 1307–1312. 10.1038/nature08947. [PubMed: 20428163]

Jiang X, Shen S, Cadwell CR, Berens P, Sinz F, Ecker AS, Patel S, and Tolias AS (2015). Principles of connectivity among morphologically defined cell types in adult neocortex. Science 350, aac9462. 10.1126/science.aac9462. [PubMed: 26612957]

Kaas JH, Lin CS, and Wagor E (1977). Cortical projections of posterior parietal cortex in owl monkeys. J Comp Neurol 72, 387–408. 10.1002/cne.901710306. [PubMed: 401839]

Kasper EM, Larkman AU, Lubke J, and Blakemore C (1994). Pyramidal neurons in layer 5 of the rat visual cortex. I. Correlation among cell morphology, intrinsic electrophysiological properties, and axon targets. J Comp Neurol 339, 459–474. 10.1002/cne.903390402. [PubMed: 8144741]

Kim EJ, Juavinett AL, Kyubwa EM, Jacobs MW, and Callaway EM (2015). Three Types of Cortical Layer 5 Neurons That Differ in Brain-wide Connectivity and Function. Neuron 88, 1253–1267. 10.1016/j.neuron.2015.11.002. [PubMed: 26671462]

Kim HG, and Connors BW (1993). Apical dendrites of the neocortex: correlation between sodium- and calcium-dependent spiking and pyramidal cell morphology. J Neurosci 13, 5301–5311. [PubMed: 8254376]

Klapoetke NC, Murata Y, Kim SS, Pulver SR, Birdsey-Benson A, Cho YK, Morimoto TK, Chuong AS, Carpenter EJ, Tian Z, et al. (2014). Independent optical excitation of distinct neural populations. Nat Methods 11, 338–346. 10.1038/nmeth.2836. [PubMed: 24509633]

Kwon SE, Yang H, Minamisawa G, and O'Connor DH (2016). Sensory and decision-related activity propagate in a cortical feedback loop during touch perception. Nat Neurosci 19, 1243–1249. 10.1038/nn.4356. [PubMed: 27437910]

Lafourcade M, van der Goes MH, Vardalaki D, Brown NJ, Voigts J, Yun DH, Kim ME, Ku T, and Harnett MT (2022). Differential dendritic integration of long-range inputs in association cortex via subcellular changes in synaptic AMPA-to-NMDA receptor ratio. Neuron 110, 1532–1546 e1534. 10.1016/j.neuron.2022.01.025. [PubMed: 35180389]

Lamme VA (1995). The neurophysiology of figure-ground segregation in primary visual cortex. J Neurosci 15, 1605–1615. [PubMed: 7869121]

Larkman A, and Mason A (1990). Correlations between morphology and electrophysiology of pyramidal neurons in slices of rat visual cortex. I. Establishment of cell classes. J Neurosci 10, 1407–1414. [PubMed: 2332787]

Larkum ME, and Nevian T (2008). Synaptic clustering by dendritic signalling mechanisms. Curr Opin Neurobiol 18, 321–331. 10.1016/j.conb.2008.08.013. [PubMed: 18804167]

Larkum ME, and Zhu JJ (2002). Signaling of layer 1 and whisker-evoked Ca2+ and Na+ action potentials in distal and terminal dendrites of rat neocortical pyramidal neurons in vitro and in vivo. J Neurosci 22, 6991–7005. 20026717. [PubMed: 12177197]

Larkum ME, Zhu JJ, and Sakmann B (1999). A new cellular mechanism for coupling inputs arriving at different cortical layers. Nature 398, 338–341. 10.1038/18686. [PubMed: 10192334]

Li LY, Ji XY, Liang F, Li YT, Xiao Z, Tao HW, and Zhang LI (2014). A feedforward inhibitory circuit mediates lateral refinement of sensory representation in upper layer 2/3 of mouse primary auditory cortex. J Neurosci 34, 13670–13683. 10.1523/JNEUROSCI.1516-14.2014. [PubMed: 25297094]

Li W, Piech V, and Gilbert CD (2004). Perceptual learning and top-down influences in primary visual cortex. Nat Neurosci 7, 651–657. 10.1038/nn1255. [PubMed: 15156149]

Llinas RR, Leznik E, and Urbano FJ (2002). Temporal binding via cortical coincidence detection of specific and nonspecific thalamocortical inputs: a voltage-dependent dye-imaging study in mouse brain slices. Proc Natl Acad Sci U S A 99, 449–454. 10.1073/pnas.012604899. [PubMed: 11773628]

Losonczy A, and Magee JC (2006). Integrative properties of radial oblique dendrites in hippocampal CA1 pyramidal neurons. Neuron 50, 291–307. 10.1016/j.neuron.2006.03.016. [PubMed: 16630839]

Lur G, Vinck MA, Tang L, Cardin JA, and Higley MJ (2016). Projection-Specific Visual Feature Encoding by Layer 5 Cortical Subnetworks. Cell Rep 14, 2538–2545. 10.1016/j.celrep.2016.02.050. [PubMed: 26972011]

Magee JC (2000). Dendritic integration of excitatory synaptic input. Nat Rev Neurosci 1, 181–190. 10.1038/35044552. [PubMed: 11257906]

Marder E, and Taylor AL (2011). Multiple models to capture the variability in biological neurons and networks. Nat Neurosci 14, 133–138. 10.1038/nn.2735. [PubMed: 21270780]

Markov NT, Vezoli J, Chameau P, Falchier A, Quilodran R, Huissoud C, Lamy C, Misery P, Giroud P, Ullman S, et al. (2014). Anatomy of hierarchy: feedforward and feedback pathways in macaque visual cortex. J Comp Neurol 522, 225–259. 10.1002/cne.23458. [PubMed: 23983048]

Martinez A, Anllo-Vento L, Sereno MI, Frank LR, Buxton RB, Dubowitz DJ, Wong EC, Hinrichs H, Heinze HJ, and Hillyard SA (1999). Involvement of striate and extrastriate visual cortical areas in spatial attention. Nat Neurosci 2, 364–369. 10.1038/7274. [PubMed: 10204544]

Mason A, and Larkman A (1990). Correlations between morphology and electrophysiology of pyramidal neurons in slices of rat visual cortex. II. Electrophysiology. J Neurosci 10, 1415–1428. [PubMed: 2332788]

McAdams CJ, and Maunsell JH (1999). Effects of attention on orientation-tuning functions of single neurons in macaque cortical area V4. J Neurosci 19, 431–441. [PubMed: 9870971]

McMains S, and Kastner S (2011). Interactions of top-down and bottom-up mechanisms in human visual cortex. J Neurosci 31, 587–597. 10.1523/JNEUROSCI.3766-10.2011. [PubMed: 21228167]

Meredith MA, Nemitz JW, and Stein BE (1987). Determinants of multisensory integration in superior colliculus neurons. I. Temporal factors. J Neurosci 7, 3215–3229. [PubMed: 3668625]

Meredith MA, and Stein BE (1983). Interactions among converging sensory inputs in the superior colliculus. Science 221, 389–391. 10.1126/science.6867718. [PubMed: 6867718]

Metherate R, and Ashe JH (1993). Ionic flux contributions to neocortical slow waves and nucleus basalis-mediated activation: whole-cell recordings in vivo. J Neurosci 13, 5312–5323. [PubMed: 8254377]

Milescu LS, Yamanishi T, Ptak K, and Smith JC (2010). Kinetic properties and functional dynamics of sodium channels during repetitive spiking in a slow pacemaker neuron. J Neurosci 30, 12113–12127. 10.1523/JNEUROSCI.0445-10.2010. [PubMed: 20826674]

Moran J, and Desimone R (1985). Selective attention gates visual processing in the extrastriate cortex. Science 229, 782–784. 10.1126/science.4023713. [PubMed: 4023713]

Morgan RJ, Santhakumar V, and Soltesz I (2007). Modeling the dentate gyrus. Prog Brain Res 163, 639–658. 10.1016/S0079-6123(07)63035-0. [PubMed: 17765743]

Morishima M, Kobayashi K, Kato S, Kobayashi K, and Kawaguchi Y (2017). Segregated Excitatory-Inhibitory Recurrent Subnetworks in Layer 5 of the Rat Frontal Cortex. Cereb Cortex 27, 5846–5857. 10.1093/cercor/bhx276. [PubMed: 29045559]

Morishima M, Morita K, Kubota Y, and Kawaguchi Y (2011). Highly differentiated projection-specific cortical subnetworks. J Neurosci 31, 10380–10391. 10.1523/JNEUROSCI.0772-11.2011. [PubMed: 21753015]

Morishima Y, Akaishi R, Yamada Y, Okuda J, Toma K, and Sakai K (2009). Task-specific signal transmission from prefrontal cortex in visual selective attention. Nat Neurosci 12, 85–91. 10.1038/nn.2237. [PubMed: 19098905]

Naka A, and Adesnik H (2016). Inhibitory Circuits in Cortical Layer 5. Front Neural Circuits 10, 35. 10.3389/fncir.2016.00035. [PubMed: 27199675]

Narayanan NS, and Laubach M (2006). Top-down control of motor cortex ensembles by dorsomedial prefrontal cortex. Neuron 52, 921–931. 10.1016/j.neuron.2006.10.021. [PubMed: 17145511]

O'Connor DH, Fukui MM, Pinsk MA, and Kastner S (2002). Attention modulates responses in the human lateral geniculate nucleus. Nat Neurosci 5, 1203–1209. 10.1038/nn957. [PubMed: 12379861]

Olcese U, Lurilli G, and Medini P (2013). Cellular and Synaptic Architecture of Multisensory Integration in the Mouse Neocortex. Neuron 79, 579–593. 10.1016/j.neuron.2013.06.010. [PubMed: 23850594]

Olson IR, Chun MM, and Allison T (2001). Contextual guidance of attention: human intracranial event-related potential evidence for feedback modulation in anatomically early temporally late stages of visual processing. Brain 124, 1417–1425. 10.1093/brain/124.7.1417. [PubMed: 11408336]

Oswald MJ, Tantirigama ML, Sonntag I, Hughes SM, and Empson RM (2013). Diversity of layer 5 projection neurons in the mouse motor cortex. Front Cell Neurosci 7, 174. 10.3389/fncel.2013.00174. [PubMed: 24137110]

Petreanu L, Mao T, Sternson SM, and Svoboda K (2009). The subcellular organization of neocortical excitatory connections. Nature 457, 1142–1145. 10.1038/nature07709. [PubMed: 19151697]

Polsky A, Mel BW, and Schiller J (2004). Computational subunits in thin dendrites of pyramidal cells. Nat Neurosci 7, 621–627. 10.1038/nn1253. [PubMed: 15156147]

Remy S, and Spruston N (2007). Dendritic spikes induce single-burst long-term potentiation. Proc Natl Acad Sci U S A 104, 17192–17197. 10.1073/pnas.0707919104. [PubMed: 17940015]

Riehle A, and Requin J (1989). Monkey primary motor and premotor cortex: single-cell activity related to prior information about direction and extent of an intended movement. J Neurophysiol 61, 534–549. 10.1152/jn.1989.61.3.534. [PubMed: 2709098]

Rockland KS, and Pandya DN (1979). Laminar origins and terminations of cortical connections of the occipital lobe in the rhesus monkey. Brain Res 179, 3–20. 10.1016/0006-8993(79)90485-2. [PubMed: 116716]

Schiller J, Major G, Koester HJ, and Schiller Y (2000). NMDA spikes in basal dendrites of cortical pyramidal neurons. Nature 404, 285–289. 10.1038/35005094. [PubMed: 10749211]

Schiller J, Schiller Y, Stuart G, and Sakmann B (1997). Calcium action potentials restricted to distal apical dendrites of rat neocortical pyramidal neurons. J Physiol 505 (Pt 3), 605–616. 10.1111/j.1469-7793.1997.605ba.x. [PubMed: 9457639]

Schulz JM, Knoflach F, Hernandez MC, and Bischofberger J (2018). Dendrite-targeting interneurons control synaptic NMDA-receptor activation via nonlinear alpha5-GABAA receptors. Nat Commun 9, 3576. 10.1038/s41467-018-06004-8. [PubMed: 30177704]

Shao Z, and Burkhalter A (1996). Different balance of excitation and inhibition in forward and feedback circuits of rat visual cortex. J Neurosci 16, 7353–7365. [PubMed: 8929442]

Shepherd GM (2013). Corticostriatal connectivity and its role in disease. Nat Rev Neurosci 14, 278–291. 10.1038/nrn3469. [PubMed: 23511908]

Snyder JS, Gregg MK, Weintraub DM, and Alain C (2012). Attention, awareness, and the perception of auditory scenes. Front Psychol 3, 15. 10.3389/fpsyg.2012.00015. [PubMed: 22347201]

Spitzer H, Desimone R, and Moran J (1988). Increased attention enhances both behavioral and neuronal performance. Science 240, 338–340. 10.1126/science.3353728. [PubMed: 3353728]

Stadler K, Bierwirth C, Stoenica L, Battefeld A, Reetz O, Mix E, Schuchmann S, Velmans T, Rosenberger K, Brauer AU, et al. (2014). Elevation in type I interferons inhibits HCN1 and slows cortical neuronal oscillations. Cereb Cortex 24, 199–210. 10.1093/cercor/bhs305. [PubMed: 23042740]

Stuart GJ, and Spruston N (2015). Dendritic integration: 60 years of progress. Nat Neurosci 18, 1713–1721. 10.1038/nn.4157. [PubMed: 26605882]

Sun YJ, Kim YJ, Ibrahim LA, Tao HW, and Zhang LI (2013). Synaptic mechanisms underlying functional dichotomy between intrinsic-bursting and regular-spiking neurons in auditory cortical layer 5. J Neurosci 33, 5326–5339. 10.1523/JNEUROSCI.4810-12.2013. [PubMed: 23516297]

Takahashi H, and Magee JC (2009). Pathway interactions and synaptic plasticity in the dendritic tuft regions of CA1 pyramidal neurons. Neuron 62, 102–111. 10.1016/j.neuron.2009.03.007. [PubMed: 19376070]

Takahashi N, Ebner C, Sigl-Glockner J, Moberg S, Nierwetberg S, and Larkum ME (2020). Active dendritic currents gate descending cortical outputs in perception. Nat Neurosci 23, 1277–1285. 10.1038/s41593-020-0677-8. [PubMed: 32747790]

Tang L, and Higley MJ (2020). Layer 5 Circuits in V1 Differentially Control Visuomotor Behavior. Neuron 105, 346–354 e345. 10.1016/j.neuron.2019.10.014. [PubMed: 31757603]

Tasic B, Yao Z, Graybuck LT, Smith KA, Nguyen TN, Bertagnolli D, Goldy J, Garren E, Economo MN, Viswanathan S, et al. (2018). Shared and distinct transcriptomic cell types across neocortical areas. Nature 563, 72–78. 10.1038/s41586-018-0654-5. [PubMed: 30382198]

Tigges J, Tigges M, and Perachio AA (1977). Complementary laminar terminations of afferents to area 17 originating in area 18 and in the lateral geniculate nucleus in squirrel monkey. J Comp Neurol 176, 87–100. 10.1002/cne.901760106. [PubMed: 409740]

Toth LJ, and Assad JA (2002). Dynamic coding of behaviourally relevant stimuli in parietal cortex. Nature 415, 165–168. 10.1038/415165a. [PubMed: 11805833]

Tran-Van-Minh A, Abrahamsson T, Cathala L, and DiGregorio DA (2016). Differential Dendritic Integration of Synaptic Potentials and Calcium in Cerebellar Interneurons. Neuron 91, 837–850. 10.1016/j.neuron.2016.07.029. [PubMed: 27537486]

Treue S, and Martinez Trujillo JC (1999). Feature-based attention influences motion processing gain in macaque visual cortex. Nature 399, 575–579. 10.1038/21176. [PubMed: 10376597]

Velez-Fort M, Rousseau CV, Niedworok CJ, Wickersham IR, Rancz EA, Brown APY, Strom M, and Margrie TW (2014). The Stimulus Selectivity and Connectivity of Layer Six Principal Cells Reveals Cortical Microcircuits Underlying Visual Processing. Neuron 84, 238. 10.1016/j.neuron.2014.09.026. [PubMed: 28898623]

Vidyasagar TR (1998). Gating of neuronal responses in macaque primary visual cortex by an attentional spotlight. Neuroreport 9, 1947–1952. 10.1097/00001756-199806220-00006. [PubMed: 9674572]

Wall NR, De La Parra M, Sorokin JM, Taniguchi H, Huang ZJ, and Callaway EM (2016). Brain-Wide Maps of Synaptic Input to Cortical Interneurons. J Neurosci 36, 4000–4009. 10.1523/JNEUROSCI.3967-15.2016. [PubMed: 27053207]

Wall NR, Wickersham IR, Cetin A, De La Parra M, and Callaway EM (2010). Monosynaptic circuit tracing in vivo through Cre-dependent targeting and complementation of modified rabies virus. Proc Natl Acad Sci U S A 107, 21848–21853. 10.1073/pnas.1011756107. [PubMed: 21115815]

Wickersham IR, Lyon DC, Barnard RJ, Mori T, Finke S, Conzelmann KK, Young JA, and Callaway EM (2007). Monosynaptic restriction of transsynaptic tracing from single, genetically targeted neurons. Neuron 53, 639–647. 10.1016/j.neuron.2007.01.033. [PubMed: 17329205]

Xu NL, Harnett MT, Williams SR, Huber D, O'Connor DH, Svoboda K, and Magee JC (2012). Nonlinear dendritic integration of sensory and motor input during an active sensing task. Nature 492, 247–251. 10.1038/nature11601. [PubMed: 23143335]

Yamashita T, and Petersen C (2016). Target-specific membrane potential dynamics of neocortical projection neurons during goal-directed behavior. Elife 5. 10.7554/eLife.15798.

Yang CR, Seamans JK, and Gorelova N (1996). Electrophysiological and morphological properties of layers V-VI principal pyramidal cells in rat prefrontal cortex in vitro. J Neurosci 16, 1904–1921. [PubMed: 8774458]

Yang W, Carrasquillo Y, Hooks BM, Nerbonne JM, and Burkhalter A (2013). Distinct balance of excitation and inhibition in an interareal feedforward and feedback circuit of mouse visual cortex. J Neurosci 33, 17373–17384. 10.1523/JNEUROSCI.2515-13.2013. [PubMed: 24174670]

Yazaki-Sugiyama Y, Kang S, Cateau H, Fukai T, and Hensch TK (2009). Bidirectional plasticity in fast-spiking GABA circuits by visual experience. Nature 462, 218–221. 10.1038/nature08485. [PubMed: 19907494]

Zhang F, Gradinaru V, Adamantidis AR, Durand R, Airan RD, de Lecea L, and Deisseroth K (2010). Optogenetic interrogation of neural circuits: technology for probing mammalian brain structures. Nat Protoc 5, 439–456. 10.1038/nprot.2009.226. [PubMed: 20203662]

Zhang S, Xu M, Kamigaki T, Hoang Do JP, Chang WC, Jenvay S, Miyamichi K, Luo L, and Dan Y (2014). Selective attention. Long-range and local circuits for top-down modulation of visual cortex processing. Science 345, 660–665. 10.1126/science.1254126. [PubMed: 25104383]

Zomorrodi R, Kroger H, and Timofeev I (2008). Modeling thalamocortical cell: impact of ca channel distribution and cell geometry on firing pattern. Front Comput Neurosci 2, 5. 10.3389/neuro.10.005.2008. [PubMed: 19129908]

Highlights

- PPC neurons receive converging monosynaptic input from frontal and sensory cortices
- L5 cell-types display distinct temporal dynamics of multimodal synaptic integration
- Cell-type specific ionic and inhibitory mechanisms shape integration timing
- Subthreshold integration dynamics translate to nonlinear action potential firing

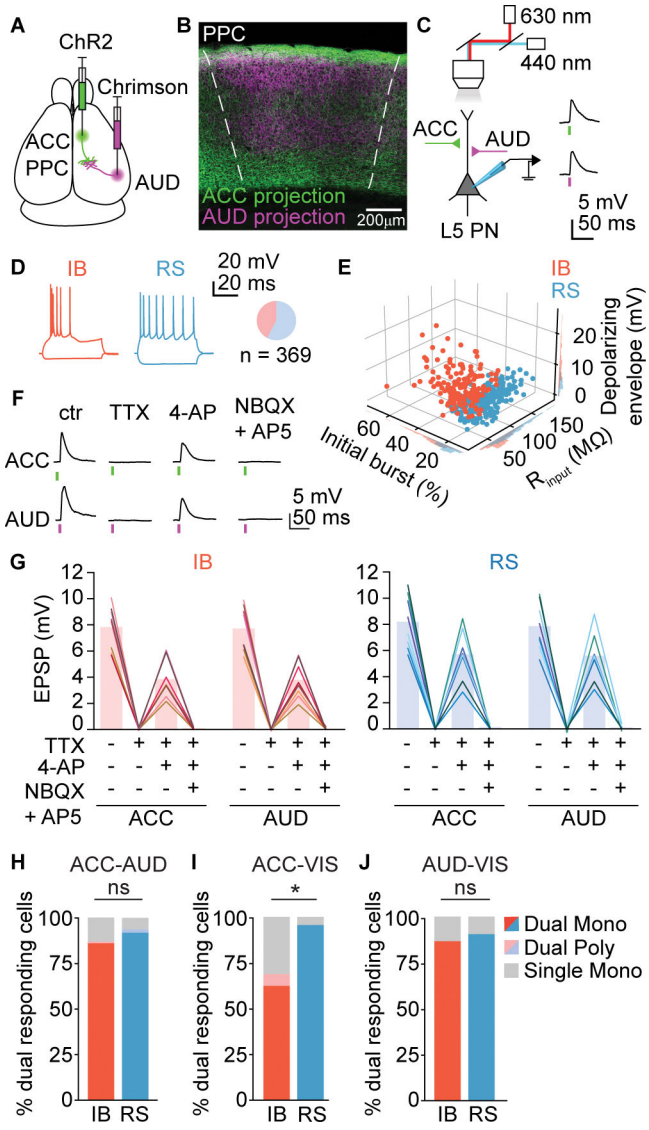

Figure 1. Dual monosynaptic innervation of layer 5 PPC neurons by feedforward and feedback afferents.

(**A**) Schematic of dual opsin transduction. (**B**) ACC and AUD afferents in the PPC. Scale bar, 200 µm. (**C**) Schematic of dual optogenetic excitation and example EPSPs. (**D**) Representative firing patterns of IB and RS neurons. Pie chart displays the proportion of IB and RS cells in PPC layer 5. (**E**) Intrinsic properties used to classify layer 5 pyramidal cells. (**F**) Determining monosynaptic connectivity using the TTX (1 µM) / 4-AP approach. Response recovery from both afferents indicates converging monosynaptic innervation. Blocking glutamatergic transmission abolishes all responses. (**G**) Response amplitudes of IB (red, n = 8) and RS (blue, n = 8) neurons in the TTX/4-AP experiment. Individual cells are represented by distinct shades of color. (**H**) Bars represent the proportion of IB and RS neurons receiving converging ACC and AUD inputs. (**I**) Proportion of neurons receiving converging ACC and VIS inputs. (**J**) Proportion of neurons receiving converging AUD and VIS inputs. *: $p < 0.05$, two-sided Fisher's exact test. See also Figures S1 and S2.

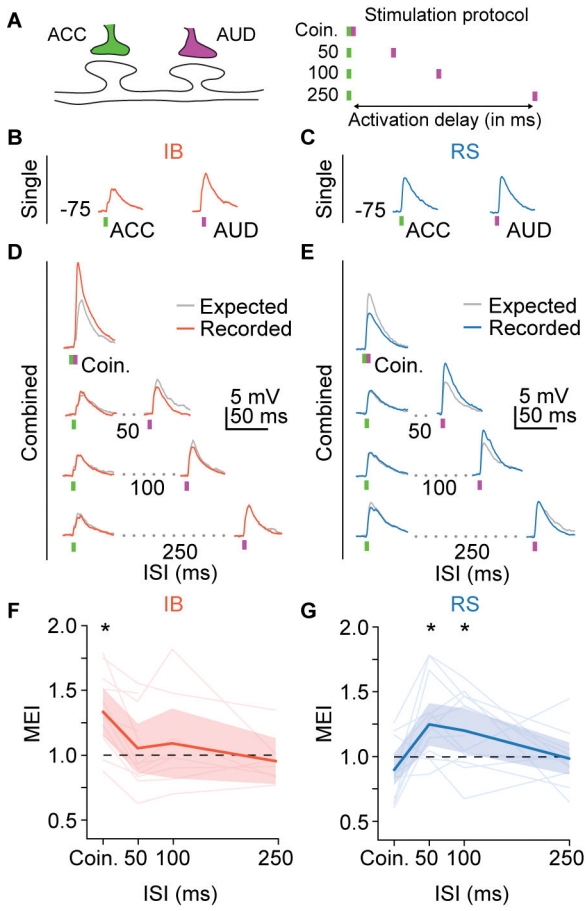

Figure 2. Cell type-specific nonlinear integration of feedforward and feedback synaptic inputs.

(**A**) Stimulation protocol in dual-innervated cells. (**B**) IB cell response to unimodal stimulation of ACC or AUD afferents. (**C**) RS cell response to unimodal stimulation of ACC or AUD afferents. (**D**) Representative IB cell responses to combined stimulation of ACC and AUD afferents. Recorded traces (red) are overlaid on the calculated linear response (grey). (**E**) Representative RS cell responses to combined stimulation of ACC and AUD afferents (blue) and the predicted linear response (grey). (**F**) Temporal dynamics of ACC-AUD integration in IB neurons (light red lines). Dark red line represents population mean; shaded area represents 95% CI. (**G**) Temporal dynamics of ACC-AUD integration in RS cells (light blue lines). Dark blue line represents population mean; shaded area represents 95% CI. Dashed black line in (F) and (G) indicates linear integration. *: $p < 0.05$, t-test. See also Figure S3.

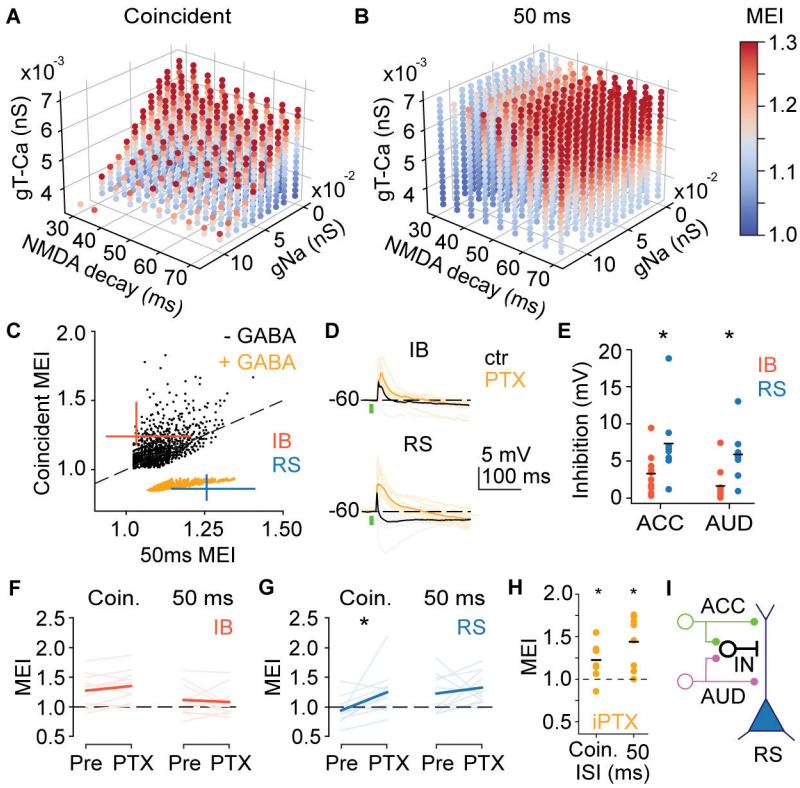

Figure 3. Temporal dynamics of nonlinear synaptic integration are determined by cell-type specific ionic conductances and feedforward inhibition.

(**A**) Simulation of coincident integration MEI values with varying Na^+ and Ca^{2+} channel conductance and NMDA receptor decay. Missing points represent values where coincident inputs drove the model past action potential threshold. (**B**) MEI values for delayed (50 ms) synaptic integration across the same parameter space as in (A). **(C**) Relationship of coincident and delayed MEI values in all models without inhibition (black dots) or with the inclusion of feedforward inhibition (orange dots). Crosshairs represent ranges of all *in vitro* recorded IB (red) and RS (blue) neurons. Error bars show 99% CI and cross at the data median. (**D**) ACC stimulation evoked EPSPs in IB (top) and RS (bottom) cells before (black) and after (orange) $GABA_A$ receptor block (PTX). (**E**) Comparison of $GABA_A$-mediated inhibition in IB (red) and RS (blue) cells. *: $p < 0.05$, unpaired t-test. (**F**) $GABA_A$ block (PTX) has no effect on ACC-AUD integration in IB cells. (**G**) $GABA_A$ block (PTX) unmasks supralinear integration of coincident inputs in RS neurons. *: $p < 0.05$, paired t-test. (**H**) MEI values measured in RS neurons with internal $GABA_A$ block (iPTX). *: $p < 0.05$, one sample t-test. (**I**) Schematic model incorporating feedforward inhibition. See also Figures S4–6.

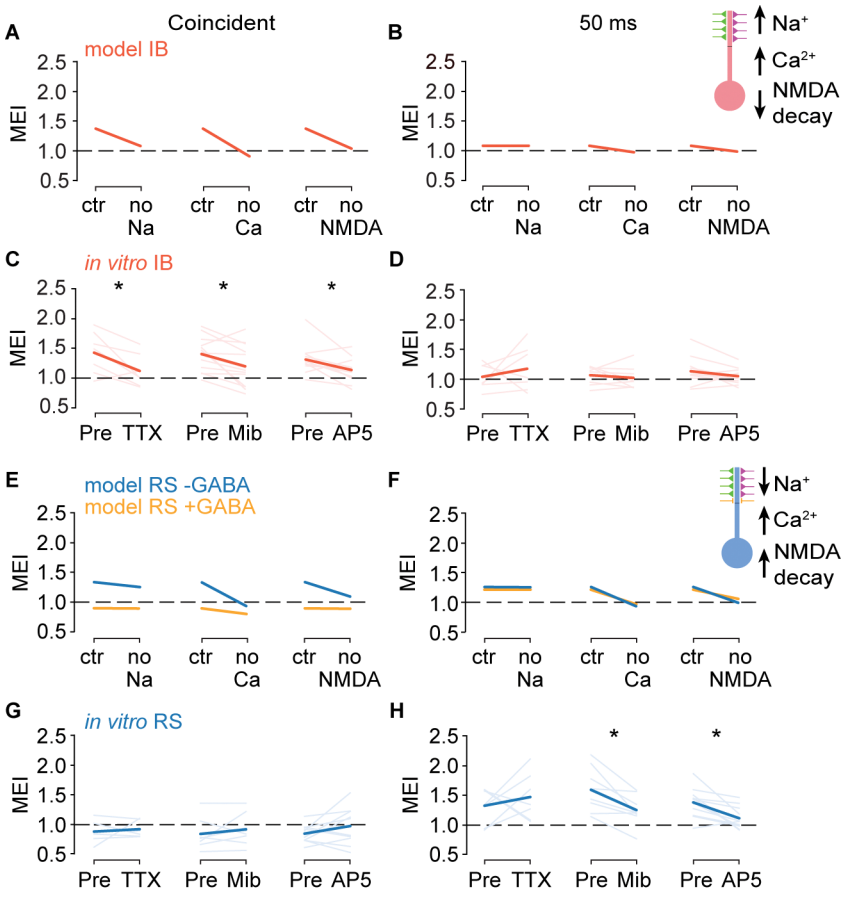

Figure 4. Pharmacological testing of model predictions.

(**A**) Simulating the effect of blocking Na^+, Ca^{2+}, or NMDA conductance on coincident integration in a model IB neuron. (**B**) Simulating the effect of blockers on delayed (50 ms) integration in a model IB neuron. Inset: schematic of model IB neurons. (**C**) *In vitro* effect of Na^+ (TTX – 100 nM), T-type Ca^{2+} (Mib) and NMDA (AP5) blockers on coincident integration in IB neurons. (**D**) The effect of pharmacological manipulations on delayed (50 ms) integration in IB neurons *in vitro*. (**E**) Simulating the effect of Na^+, Ca^{2+} or NMDA block on coincident integration in a model RS neuron with (orange) or without (blue) feedforward inhibition. (**F**) Simulating the effect of Na^+, Ca^{2+} or NMDA block on delayed (50 ms) integration in model RS neurons. Inset: schematic of model RS neurons. (**G**) *In vitro* effect of Na^+ (TTX – 100 nM), T-type Ca^{2+} (Mib) and NMDA (AP5) blockers on coincident integration in RS neurons. (**H**) The effect of pharmacological manipulations on delayed (50 ms) integration in RS neurons *in vitro*. *: $p < 0.05$, paired t-test. See also Figure S7.

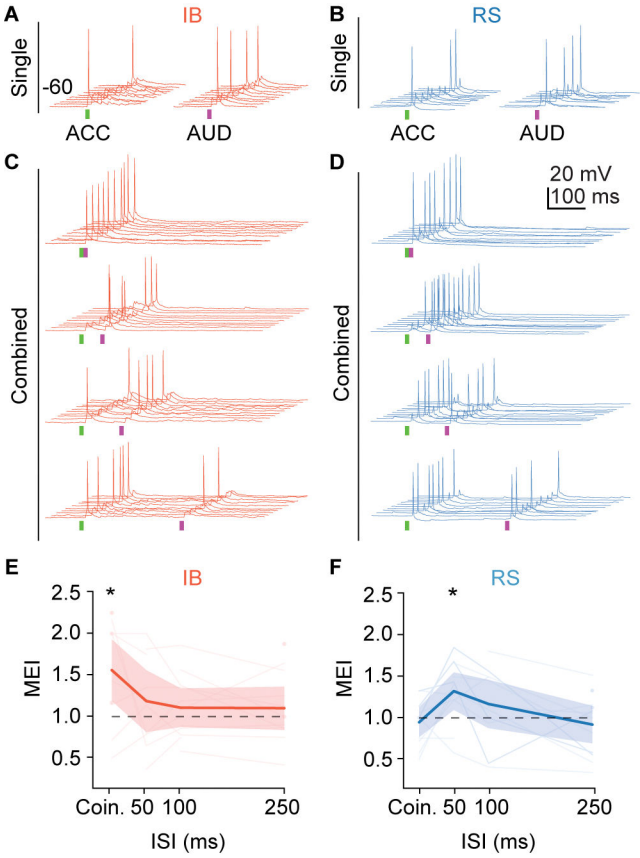

Figure 5. Temporal dynamics of action potential output mimic subthreshold feedforward-feedback integration dynamics.

(**A**) Action potential firing of an IB cell (red) in response to unimodal stimulation. (**B**) Unimodal firing responses in an RS cell (blue). (**C**) Action potential firing in response to combined ACC-AUD stimulation at different delays, same IB cell as in (A). (**D**) RS cell action potential firing in response to combined stimulation, same cell as in (B). (**E**) Temporal dynamics of suprathreshold ACC-AUD integration in IB neurons (light red lines). (**F**) Temporal dynamics of suprathreshold ACC-AUD integration in RS cells (light blue lines). Dark lines in (E) and (F) represent population means; shaded areas represent 95% CI. Dashed black lines indicate linear integration. *: $p < 0.05$, t-test.

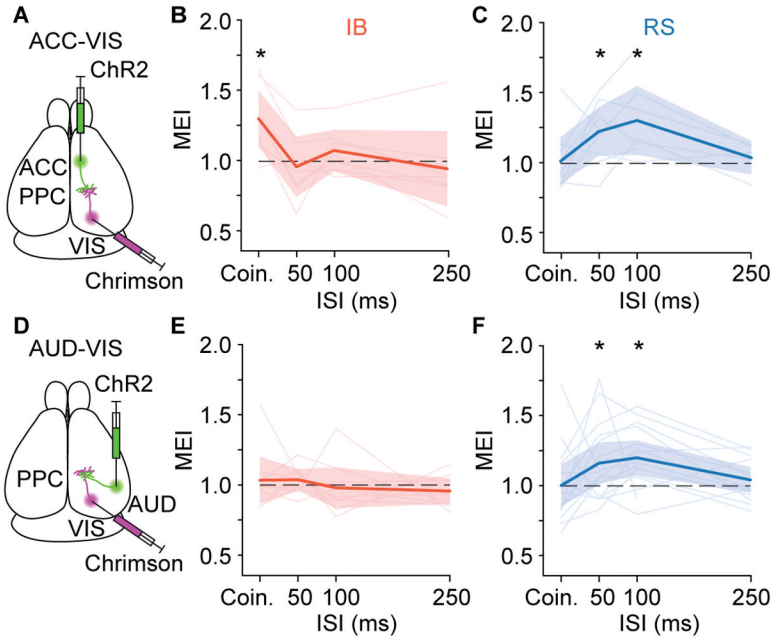

Figure 6. Input specificity of nonlinear synaptic interactions differs between IB and RS cells.

(**A**) Schematic of ACC and VIS dual opsin transduction. (**B**) Temporal dynamics of ACC-VIS integration in IB neurons (light red lines). (**C**) Temporal dynamics of ACC-VIS integration in RS neurons (light blue lines). (**D**) Schematic of AUD and VIS dual opsin transduction. (**E**) Temporal dynamics of AUD-VIS integration in IB neurons (light red lines). (**F**) Temporal dynamics of AUD-VIS integration in RS neurons (light blue lines). Dark lines in panels (B), (C), (E), and (F) represent population means; shaded areas represent 95% CI. Dashed black lines indicate linear integration. *: $p < 0.05$, t-test.

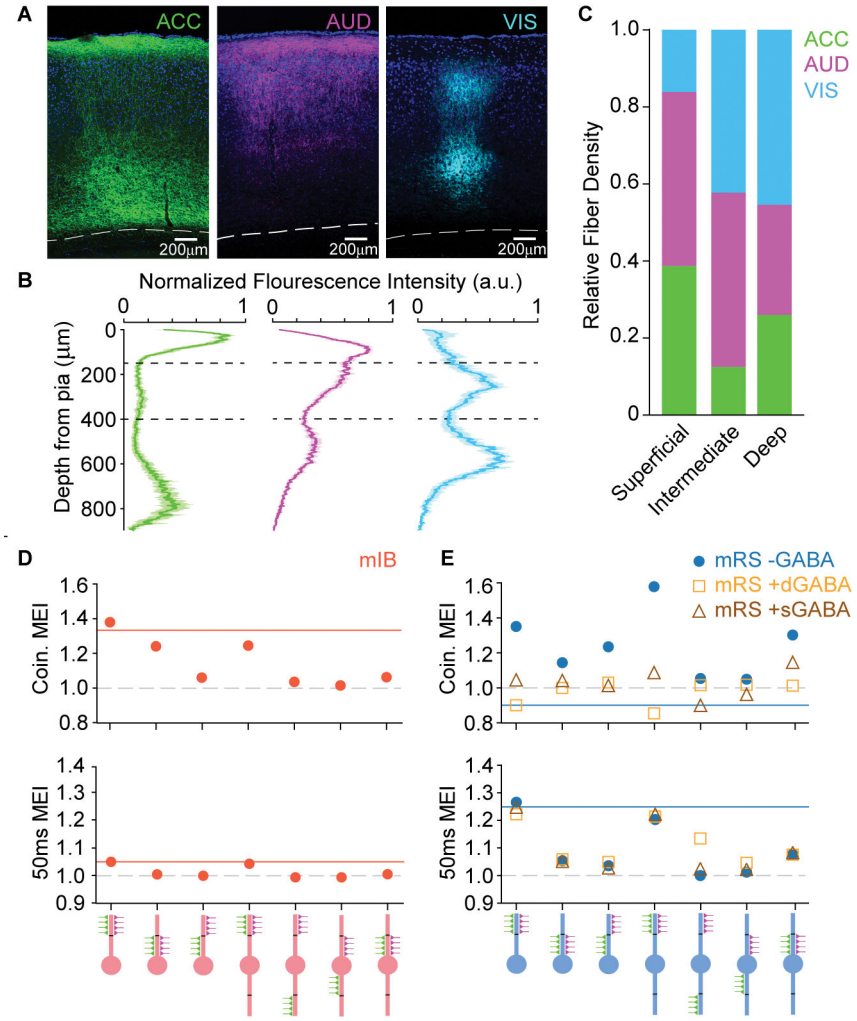

Figure 7. Synapse location plays a key role in nonlinear interactions.

(**A**) Confocal images of ACC (green), AUD (magenta) and VIS (cyan) projections to the PPC. Blue: DAPI staining, scale bars are 200 μm. (**B**) Histograms showing the distribution (mean ± SEM) of ACC (n = 9), AUD (n = 16) and VIS (n = 7) fibers. (**C**) Relative density of ACC, AUD, and VIS fibers in superficial (0–150 μm from the pial surface), intermediate (150–400 μm) and deep (400–800 μm) sections of the PPC cortical column. (**D**) Simulated synaptic integration performance of IB neuron models (red) across various anatomical configurations. (**E**) Simulated synaptic integration in RS neuron models without inhibition (−GABA, blue dots), with inhibition arriving at the same dendritic segment as excitation (+dGABA, orange squares), or with somatic inhibition (+sGABA, brown triangles) across anatomical configurations. In panels (D) and (E), multimodal enhancement index (MEI) was measured for coincident (top) and delayed (50 ms, bottom) activation of excitatory inputs. Solid red and blue lines indicate experimentally measured MEIs. Unimodal EPSP magnitudes were matched across model configurations. See also Figures S8 and S9.

KEY RESOURCES TABLE

REAGENT or RESOURCE	SOURCE	IDENTIFIER
Antibodies		
Bacterial and virus strains		
AAV2.1-hSyn-hChR2(H134R)-EYFP	Zhang et al. (2010)	Addgene 26973-AAV1
AAV2.9-hSyn-hChR2(H134R)-EYFP	Zhang et al. (2010)	Addgene 26973-AAV9
AAV2.1-Syn-ChrimsonR-tdTomato	Klapoetke et al. (2014)	Addgene 59171-AAV1
AAV2.9-Syn-ChrimsonR-tdTomato	Klapoetke et al. (2014)	Addgene 59171-AAV9
AAVrg-hSyn-mCherry	Zhang et al. (2010)	Addgene 114472-AAVrg
pENN.AAVrg.hSyn.Cre.WPRE.hGH	Cearley et al. (2008)	Addgene 105553-AAVrg
Biological samples		
Healthy mouse brain tissue	This paper	N/A
Chemicals, peptides, and recombinant proteins		
Tetrodotoxin citrate	Tocris	Cat. #1069/1
Mibefradil dihydrochloride	Tocris	Cat. #2198/10
D-AP5	Tocris	Cat. #0106/1
Picrotoxin	Tocris	Cat. #1128/1G
NBQX disodium salt	Tocris	Cat. #1044/1
QX 314 Bromide	HelloBio	Cat. #HB1029
4-Aminopyridine (4-AP)	Tocris	Cat. #0940
NeuroTrace™ 435/455 Blue Fluorescent Nissl Stain	ThermoFisher	Cat. #N21479
Cholera Toxin Subunit B (Recombinant), Alexa Fluor™ 488 Conjugate	ThermoFisher	Cat. #C34775
Cholera Toxin Subunit B (Recombinant), Alexa Fluor™ 555 Conjugate	ThermoFisher	Cat. # C22843
Critical commercial assays		
Deposited data		
AMPA NMDA receptor model objects for receptor currents and kinetics used in computational modeling	Egger et al. (2015)	https://senselab.med.yale.edu/ModelDB/ShowModel?model=167499#tabs-1
$GABA_AR$ receptor model objects for receptor currents and kinetics used in computational modeling	Egger et al. (2015)	https://senselab.med.yale.edu/ModelDB/ShowModel?model=167499#tabs-1
T-type calcium channel model objects for channel currents and kinetics used in computational modeling	Destexhe et al. (1998)	https://senselab.med.yale.edu/ModelDB/ShowModel?model=279#tabs-1
HCN1 channel model objects for channel currents and kinetics used in computational modeling	Stadler et al. (2014)	https://senselab.med.yale.edu/ModelDB/ShowModel?model=168148#tabs-1
Sodium and Potassium channel model objects for channel currents and kinetics used in computational modeling	Morgan et al. (2007)	https://senselab.med.yale.edu/ModelDB/ShowModel?model=124513#tabs-1
Calcium-activated potassium channel model objects for channel currents and kinetics used in computational modeling	Morgan et al. (2007)	https://senselab.med.yale.edu/ModelDB/ShowModel?model=124513#tabs-1
Experimental models: Cell lines		
Experimental models: Organisms/strains		
Mouse: C57BL/6J wildtype	The Jackson Laboratory	JAX: 000664
Mouse: Ai14 reporter line	The Jackson Laboratory	JAX: 007914

REAGENT or RESOURCE	SOURCE	IDENTIFIER
Oligonucleotides		
Recombinant DNA		
Software and algorithms		
Python version 3.7	Python Software Foundation	https://www.python.org
WaveSurfer	HHMI Janelia Research Campus	https://www.janelia.org/open-science/wavesurfer
NEURON	Hines and Carnevale (1997)	https://neuron.yale.edu/neuron/
Prism 8	GraphPad	https://www.graphpad.com/
ImageJ	NIH	https://imagej.net/software/fiji/
Analysis pipelines related to multimodal sub- and suprathreshold synaptic integration	This paper	https://github.com/LurLab-UCI/Rindner-et-al.-2022
Compartmental model	This paper	http://modeldb.yale.edu/267509
Other		
Sutter Instruments TLED+ (440nm, 620nm)	Sutter Instruments	TLEDPLUS-Y
Lambda optical beam combiner	Sutter Instruments	LB-OBC-Y
Pipette puller	Sutter Instruments	P-1000
Vibrating microtome	Campden Instruments	smz7000-2
MultiClamp amplifier	Molecular Devices	MultiClamp 700B
DAQ board	National Instruments	NI-6353
Zeiss LSM900	UCI BioSci OBC	Zeis